inventions

MDPI

Article

A Thermodynamic Model for Lithium-Ion Battery Degradation: Application of the Degradation-Entropy Generation Theorem

Jude A. Osara * and Michael D. Bryant

Mechanical Engineering Department, University of Texas at Austin, Austin, TX 78712, USA; bryantmd@austin.utexas.edu

* Correspondence: osara@utexas.edu

Received: 19 February 2019; Accepted: 27 March 2019; Published: 3 April 2019

Abstract: Presented is a lithium-ion battery degradation model, based on irreversible thermodynamics, which was experimentally verified, using commonly measured operational parameters. The methodology, applicable to all lithium-ion batteries of all chemistries and composition, combined fundamental thermodynamic principles, with the Degradation–Entropy Generation theorem, to relate instantaneous capacity fade (loss of useful charge-holding capacity) in the lithium-ion battery, to the irreversible entropy generated via the underlying dissipative physical processes responsible for battery degradation. Equations relating capacity fade—aging—to battery cycling were also formulated and verified. To show the robustness of the approach, nonlinear data from abusive and inconsistent battery cycling was measured and used to verify formulations. A near 100% agreement between the thermodynamic battery model and measurements was achieved. The model also gave rise to new material and design parameters to characterize all lithium-ion batteries.

Keywords: lithium-ion battery; battery aging; degradation analysis; entropy generation; capacity fade; voltage temperature; thermodynamics

1. Introduction

Lithium-ion batteries are rechargeable and exhibit high-energy density, minimal maintenance, low self-discharge, and a long cycle life [1,2]. Lithium-ion battery issues include self-discharge, aging and thermal instability. Models to predict performance over time, use electrical parameters and theories, others combine electrical and chemical phenomena [1–4]. Although significant advances have been made for battery electrode and electrolyte materials [4–7] for high-energy density lithium-ion batteries, critical issues concerning safety, reliability, and continuous availability [5,8–11] limit their use. To mitigate loss of charge-storing capacity with cycling, and to prevent battery overheating, leading to catastrophic thermal events, manufacturers of lithium-ion battery-operated devices and electric vehicles often rely on computationally intensive monitoring algorithms [11,12], which are unreliable at predicting sudden battery instabilities/failures. Due to the complex internal mechanisms involved in the lithium-ion battery operation, battery manufacturers and researchers use expensive empirically fitted mathematical models to estimate the battery's response to loading [13–16]. Needed is a robust and universal model to accurately and consistently characterize the battery and predict degradation under all operating conditions, irrespective of active mechanisms or interactions. Presented is an entirely physics-based battery degradation model that instantaneously characterizes the battery's response, using commonly measured battery parameters of voltage, current, and temperature.

The chemistries at the battery's cathode [7]

$$Li_{1-x}MO_2 + xLi^+ + xe^- \rightleftharpoons LiMO_2 \quad (1)$$

and anode [7]

$$Li_xC_6 \rightleftharpoons C_6 + xLi^+ + xe^- \quad (2)$$

give an overall cell reaction [9]

$$Li_{1-x}MO_2 + Li_xC_6 \rightleftharpoons LiMO_2 + C_6 \quad (3)$$

involving a nominal cell voltage of approximately 3.6–4.2 V, depending on the transition metal M used. Here, $0 \leq x < 1$. Transition metals include cobalt, manganese, and nickel, among others. In a typical Li-ion cell, the electrodes are active materials $Li_{1-x}MO_2$ and Li_xC_6, bonded to current collectors by the electrolyte, usually liquid, gel, or lithium metal polymer, which facilitates transport of lithium ions (Li^+) between electrodes. During charging, Li^+ are deintercalated (extracted) at the cathode and the active material is oxidized, whereas the anode active material is reduced and Li^+ extracted from the cathode are intercalated (inserted) into the anode. The phenomena reverse for discharge [1,4,7].

Full charging applies a constant current which energizes the battery to its rated voltage, followed by a constant-voltage process during which charge current decreases to 1–3% of the battery's rated current. Cycling a battery dissipates a variable amount of heat, depending on the discharge/charge rates and operating conditions. End of discharge voltage for typical commercial Li-ion batteries is 2.7 V/cell, to avoid damage from deep discharge. An intermediate step, settling, allows the transport phenomena and reaction kinetics to stabilize. Manufacturers specify nominal and typical electrical charge-holding capacity (discharge capacity) of Li-ion batteries at a given discharge rate (or current) in Ampere-hours (Ah).

Battery life, typically 500 to 1200 discharge–charge cycles, depends on many factors [8–10]. Even with proper maintenance, the capacity of a Li-ion cell fades with cycling. Several discharge–charge cycles produce more dissipative losses which generate heat [1]. Other degradation mechanisms include lithium corrosion and plating on the anode, and excessive growth or disconnection of the solid–electrolyte interface (SEI) layer on or from the anode, respectively, resulting in a loss of contact [10]. On the cathode, a passivation layer forms, which grows during cycling and reduces capacity over time. Structural changes in the electrodes and irreversible decomposition of the electrolyte over time also limit intercalation and diffusion of Li^+.

Li-ion batteries are very sensitive to charge rates and Depth of Discharge DoD. Improper charging overheats batteries, causing catastrophic failure. Overcharging facilitates migration of Li^+ from the layered structure, building up metallic lithium on the anode and releasing excess oxygen at the cathode. As this continues, pressure in the battery increases and more heat is released, which can eventually cause an explosion. Overdischarging causes similar irreversible damage. Battery capacity and life cycle also depend on design and operating conditions.

Background/Literature Review

In [16,17], lithium-ion battery degradation in electric vehicle application is presented. In both studies, the authors used empirically fitted Thevenin (for battery characterization) and DoD-dependent (for battery aging) models. Using representative real-world drive cycles, a close fit between model and experimental results was obtained [16], while noting the effects of regenerative braking and ambient temperature on model error. In [17], consistent cycling capacity fade test of a 200 Ah lithium-ion battery yielded a model accuracy greater than 96.5%, for all 400 cycles.

Karnopp [18] coupled the chemical and electrical interactions of a battery via the Gibbs relation $A\,J = \sum \mu_i \dot{N}_i = -\dot{G}$ where A is de Donder's affinity, J is reaction rate, μ_i are chemical potentials, N_i are numbers of moles, and G is Gibbs free energy. The dot above quantities represents differentiation with time t. The entropy produced $S\prime$ from the energy dissipated via the Ohmic or chemical reaction, was evaluated from Prigogine's minimum entropy generation theorem [19] as

$$\dot{S}\prime = \frac{A\,J}{T} = \frac{VI}{T} \quad (4)$$

where T is temperature, V is battery voltage, I is battery current, and the apostrophe denotes entropy production. In [20], process irreversibilities in lithium-ion batteries were presented through overpotentials (charge transfer and diffusion). The authors gave a thermodynamic model using Gibbs energy change

$$dG = -S_{rev}dT + \mathcal{V}dP + Vdq \tag{5}$$

where $S_{rev} = -\left(\frac{\partial G}{\partial T}\right)_P = q\left(\frac{\partial V}{\partial T}\right)$ was the reversible entropy from thermal energy change. The irreversible entropy produced by the Ohmic work dissipation was $\dot{S}\prime = \frac{VI}{T}$ and the entropy transfer out was $\dot{S}_{ext} = \frac{hA(T_\infty - T)}{T}$. Menard et al. [3] gave a similar bond-graph model for one electrode of the lithium-ion battery.

While measurements of temperature-dependent degradation are readily available [10,15,21–27], models do not adequately estimate the effect of temperature on battery performance. Some use the Arrhenius equation to model temperature-dependent degradation at moderate to high temperatures, and empirical models for lower temperatures [15,22–27]. Battery degradation models, not valid for all instantaneous conditions, often fail under unsteady operation, deep discharge, or other nonlinear system interactions; often cannot accurately predict useful life; cannot adequately account for battery aging or parasitic losses; and cannot be easily adapted to other battery types. This study used thermodynamic formulations (of irreversible entropies produced as a consequence of energy dissipation) and the DEG theorem [28], to analyze nonlinear, uncontrolled and cyclically inconsistent lithium-ion battery degradation. Since these entropies in turn depend on those phenomenological parameters (or variables) used by the battery industry to describe degradation, the result was a battery degradation model, based on fundamentals, but expressed in terms of convenient industry parameters. The analyses were then experimentally verified. Definitions of relevant battery parameters were adapted from [1].

2. Degradation-Entropy Generation Theorem Review

Rayleigh [29] through his dissipation function was the first to characterize dissipative forces. In classical irreversible thermodynamics, Onsager [30] developed his famous reciprocity theorem [19]. A quantitative study of degradation of systems through dissipative processes, by Bryant et al. [28], formulated the Degradation-Entropy Generation (DEG) theorem, that established a direct relationship between degradation measure w (which in this article is battery charge content or capacity) and rates of entropy generation $S\prime_i$, using irreversible thermodynamics. Entropy measures disorganization in materials. Since degradation is advanced and permanent disorganization, entropy generation is fundamental to degradation.

2.1. Statement

Given an irreversible material transformation consisting of $i = 1, 2, \ldots, n$ dissipative processes p_i, which could describe an energy, work, or heat characteristic of the process, and assuming the mechanism can be described by a parameter or state variable w that measures the effects of the transformation or degradation, such that

$$w = w(p_i) = w(p_1, p_2, \ldots, p_n),\ i = 1, 2, \ldots, n \tag{6}$$

is monotonic in each p_i. Then the rate of change of the degradation

$$\dot{w} = \sum_i B_i \dot{S}\prime_i \tag{7}$$

is a linear combination of rates of entropies $\dot{S}\prime_i$ generated by the dissipative processes p_i, where the transform process coefficients

$$B_i = \left.\frac{\partial w}{\partial S\prime_i}\right|_{p_i} \tag{8}$$

are slopes of degradation w with respect to entropy generation $S\prime_i$; the $\big|_{p_i}$ notation refers to the process p_i being active.

The theorem was stated and proved in [28]. Integrating Equation (7) over time t, composed of cycles wherein B_i is constant, yields the accumulated total degradation

$$\Delta w = \sum_i B_i S\prime_i \tag{9}$$

which is a linear combination of the accumulated entropies $S\prime_i$ generated by the dissipative processes p_i.

2.2. Generalized Degradation Analysis Procedure

Bryant et al. [28] presented a structured approach to degradation analysis which embeds the physics of the dissipative processes into the energies $p_i = p_i\left(\zeta_{ij}\right),\ j = 1, 2, \ldots, m$; derives entropy generation $\dot{S}\prime_i$ as a function of the p_i and expresses the rate of degradation $\dot{w}$, as a linear combination of the entropy generation terms, Equation (7). p_i is the energy dissipated by internal processes, lost work, transferred heat, a change in the thermodynamic energy (internal energy, enthalpy, Helmholtz or Gibbs free energy), or some other functional form of energy. ζ_{ij} are the time-dependent phenomenological variables used in practice and associated with p_i. The degradation/transform coefficients B_i must be measured using Equation (8). This approach has the following characteristics:

- It identifies the degradation measure w, dissipative process energies p_i, and phenomenological variables ζ_{ij};
- It finds the entropy generation $S_i\prime = S_i\prime(p_i)$ caused by the dissipative processes p_i;
- It evaluates the coefficients B_i by measuring increments, accumulation or rates of degradation versus increments, accumulation or rates of entropy generation;
- It relates degradation measure to entropy generation, via Equations (7) or (9).

This approach can formulate degradation models consisting of one or many dissipative processes p_i, acting simultaneously. The DEG theorem has been previously applied to friction and wear processes [31–34] and metal fatigue [35–37].

3. Formulations

3.1. Fundamental Thermodynamic Formulations

This section reviews the laws of thermodynamics [19,38–44].

3.1.1. First Law—Energy Conservation

The first law of thermodynamics

$$dU = \delta Q - \delta W + \sum \mu_k dN_k \tag{10}$$

for a stationary thermodynamic system, neglecting gravity, dU balances the change in internal energy, δQ is the heat exchange across the system boundary, δW is sum of the work transfer across the system boundary, and $\sum \mu_k dN_k$ is sum of the compositional energy changes. Inexact differential δ indicates path-dependent variables.

3.1.2. Second Law and Entropy Balance—Irreversible Entropy Generation

The Clausius inequality is the change in entropy for a closed system:

$$dS \geq \frac{\delta Q}{T} \tag{11}$$

The inequality indicates the system's entropy change dS equals or exceeds the measured entropy transfer by heat $\delta Q/T$, across the system boundary. For a reversible process, the entropy change

$$dS = dS_{rev} = \frac{\delta Q_{rev}}{T} \tag{12}$$

which approximates a quasi-static (very slow) process, in which total entropy change occurs via a reversible heat transfer δQ_{rev}.

Expressed as the equality $dS = dS_e + \delta S'$ by Prigogine [19,42], the second law of thermodynamics equates dS to the measured entropy flow dS_e across the system boundaries from heat transfer or mass transfer (for open systems), plus any entropy $\delta S'$ produced through dissipative processes, within the system boundaries. Entropy generation $\delta S'$ measures the structural disorganization from permanent changes to the system [19,40,42,45], when it evolves. For a closed system (no mass transfer across system boundaries), the second law becomes [19,42]

$$dS = dS_{irr} = \frac{\delta Q}{T} + \delta S' \tag{13}$$

where dS_{irr} is entropy change along an irreversible (real) path, $\delta Q/T$ is entropy flow by heat transfer, which might be positive or negative, and T is the temperature of the boundary where the energy/entropy transfer takes place. The second law, via Equations (11) and (13), also asserts that entropy generation $\delta S' \geq 0$.

3.1.3. Combining First and Second Laws

Reversible Transformation: For a system undergoing quasi-static heat transfer and compression work, Equation (10), replacing δQ with $\delta Q_{rev} = TdS_{rev}$ from Equation (12), gives the combined form of the first and second laws [44]

$$dU = dU_{rev} = TdS_{rev} - Pd\mathcal{V} + \sum \mu_k dN_k \tag{14}$$

Here P is pressure, $\mathcal{V}$ is volume, and T is temperature. Equation (14) is the reversible change in internal energy between two equilibrium states according to the first law, and is valid for all systems.

Irreversible Transformation: Eliminating δQ from Equation (10) via Equation (13) gives, for compression work $Pd\mathcal{V}$, [19,33,34,41,42]

$$dU = dU_{irr} = TdS_e - T\delta S' - Pd\mathcal{V} + \sum \mu_k dN_k \tag{15}$$

the irreversible combined first and second laws. Equation (15) applies to irreversible processes. Comparing to the prior equation, reversible entropy change dS_{rev} was replaced by entropy flow dS_e, and entropy generation $\delta S'$ was included.

3.2. Li-Ion Battery Analysis

Battery degradation observed electrically via capacity fade, occurs chemically through electrode corrosion and evolution of gases, and thermally through hot surroundings and joule heating.

Engineering Model: The thermodynamic system boundary only encloses the battery; the system is closed (battery mass stays in the battery); heat transfers between battery and surroundings; and the system is at equilibrium before and after charging or discharging.

3.2.1. Combining First and Second Laws with Gibbs Potential

Electrochemical energy storage devices are conveniently characterized using the Gibbs free energy [19,40,42,45]

$$G = U + P\mathcal{V} - TS \tag{16}$$

which measures process-initiating energy changes in a thermodynamic system. Differentiating Equation (16) and substituting Equation (14) for dU into the result, give the Gibbs fundamental relation

$$dG = dG_{rev} = -S_{rev}dT + \mathcal{V}dP + \sum \mu_k dN_k \leq 0 \tag{17}$$

the quasi-static (reversible) change in Gibbs energy of the system between two equilibrium states according to the first law, valid for all systems. At constant pressure $dP = 0$,

$$dG = dG_{rev} = -S_{rev}dT + \sum \mu_k dN_k \leq 0 \tag{18}$$

where $dG = dG_{rev}$ is the free energy change in the battery, via the reversible (rev) path, maximum for energy transfer out of the battery (discharge), and minimum for energy transfer into the battery (charge). For reactions such as phase transitions and chemical formation/decomposition of substances, change in the Gibbs energy via reversible and irreversible paths, between states, can be used to calculate entropy change in the process.

Embedded in the compositional energy change term $\sum \mu_k dN_k$ are the battery's electrochemical kinetics, which include mass change due to chemical reactions $dN^r{}_k$, mass flow across system boundary $dN^e{}_k$, and ionic diffusion of mass within the system boundary $dN^d{}_k$, i.e., $dN_k = dN^r{}_k + dN^e{}_k + dN^d{}_k$, where N_k is the number of moles of material species k with $N^r{}_k$, $N^e{}_k$, and $N^d{}_k$ the reactive, externally transferred and internally diffusive species, respectively. For a battery (closed system), $dN^e{}_k = 0$ gives $dN_k = dN^r{}_k + dN^d{}_k$, and

$$\sum \mu_k dN_k = \sum \mu^r_k dN^r{}_k + \sum \left(\mu_{high} - \mu_{low}\right) dN^d{}_k \tag{19}$$

accounts for chemical reactions r and diffusion d (note superscripts). Variation in chemical potential within the battery induces diffusion, hence μ_{high} and μ_{low} are chemical potentials in the high- and low-potential regions, respectively [19,42], and $dN^d{}_k$ is the amount of active species transported between both regions. Considering the source of the battery's electrical energy is chemical and ionic, the reaction and diffusion terms in Equation (19) are replaced by the directly coupled electrical boundary work Vdq, such that

$$\sum \mu_k dN_k = Vdq \tag{20}$$

where V is the terminal voltage and $dq = Idt$ is the charge transferred by battery current I over time dt. The derivations that convert Equation (19) to (20), which couple the electrochemical kinetics to the easily measured V and I, are given in Appendix A. The change in Gibbs free energy (Equation (18)) becomes, for the discharge/charge process,

$$dG = dG_{rev} = -S_{rev}dT + Vdq \leq 0 \tag{21}$$

Differentiating Gibbs energy Equation (16) with the pressure constant and substituting Equation (15) for dU into the result, give the irreversible form of the Gibbs relation

$$dG = \delta G_{irr} = -SdT + Vdq - T\delta S\prime \leq 0 \tag{22}$$

where $dG = \delta G_{irr}$ is the free electrochemical energy change in the battery, via the irreversible (irr) path, also maximum for energy transfer out of the battery (discharge) and minimum for energy transfer into the battery (charge). In Equation (22), by singling out the first two terms, the phenomenological Gibbs energy change can be defined as

$$\delta G_{phen} = -SdT + Vdq \tag{23}$$

due, only, to the changes in the physically observable and measurable intensive and extensive state variables (dT and dq are easily measured). Note the overall change dG can be evaluated via a constant ideal change, dG_{rev} (Equation (21)), for a reversible process, or via a nonlinear, irreversible, and

path-dependent real change, dG_{irr} (Equation (22))—both assess the total change in Gibbs free energy. With dG between beginning and end states known via dG_{rev}, Equations (21) and (22) can be combined to introduce the battery's fundamental Gibbs-based entropy generation or production at constant pressure

$$\delta S\prime = -\frac{SdT}{T} + \frac{Vdq}{T} - \frac{dG_{rev}}{T} = \frac{\delta G_{phen}}{T} - \frac{dG_{rev}}{T} \geq 0 \tag{24}$$

which satisfies the first and second laws. Equation (24) evaluates entropy generation $\delta S\prime$ via the difference between Gibbs energy changes between two thermodynamic states, along reversible and phenomenological paths. During discharge (energy extraction), $dT \geq 0, dq \leq 0$ and $dG_{rev} \leq 0$, rendering $\delta S\prime \geq 0$. For charge (energy addition), $dT \leq 0,\ dq \geq 0$ and $dG_{rev} \geq 0$, reversing the signs of the middle terms in Equation (24) to preserve accordance with the second law: $\delta S\prime \geq 0$ [42]. In batteries, dG_{rev} can be evaluated via

$$dG_{rev} = V_{OC} dq_{rev} \tag{25}$$

where V_{OC} is the battery's standard potential (or open-circuit voltage) and dq_{rev} is reversible charge transfer.

Equation (24) defines entropy production as the difference between phenomenological Gibbs entropy $dS_{phen} = \frac{\delta G_{phen}}{T} = -\frac{SdT}{T} + \frac{Vdq}{T}$ and reversible (ideal) Gibbs entropy $dS_{rev} = \frac{dG_{rev}}{T}$, restated as

$$\delta S\prime = \delta S_{phen} - dS_{rev} \geq 0 \tag{26}$$

where $(dS_{rev} \leq \delta S_{phen}) < 0$ for discharge and $0 < (dS_{rev} \leq \delta S_{phen})$ for charge, making Equation (26), a statement of the second law, universally consistent with the thermodynamic process directional signs (IUPAC convention of positive energy into a system and negative work out).

Comparing Equations (12) to (13), and (21) to (22), and recalling the thermodynamic State Principle, shows that the changes in Gibbs entropy and energy between the two states are path-independent, whether the process path is reversible or irreversible, i.e.,

$$dS = dS_{rev} = \delta S_{irr} = \delta S_{phen} - \delta S\prime,\ dG = dG_{rev} = \delta G_{irr} = \delta G_{phen} - T\delta S\prime \tag{27}$$

Entropy and energy changes along an irreversible path must sum the instantaneously observed/measured phenomenological entropy and energy changes to the internally generated entropy and energy loss. Most battery analyses use reversible Gibbs energy change $dG = dG_{rev}$ and entropy change $dS = dS_{rev}$ [46,47]—only end-state measurements of system variables (before and after a discharge or charge step) are required, unlike $dG = \delta G_{irr} = \delta G_{phen} - T\delta S\prime$ and $dS = \delta S_{irr} = \delta S_{phen} - \delta S\prime$, which require instantaneous accounting of all active processes. Since dG and dS during a process can be negative or positive, depending on heat flow TdS_e or entropy flow dS_e into or out of the battery, neither dG nor dS measures the permanent changes in the battery. On the other hand, entropy generation, Equation (24) or (26), evolves monotonically as per the second law. With $\delta S\prime = 0$ indicating an ideal (reversible) battery-process interaction, Equation (26) also indicates that a portion of any real battery's energy is never available for external work, $\delta S\prime > 0$. In Equation (26), the entropy generated by the battery's internal irreversibilities alone, is in accordance with experience, similar to the Gouy-Stodola theorem used in availability (exergy) analysis [43,45,48,49]. Note since a discharged battery cannot 'revert' to a charged state without external recharging, all batteries are thermodynamically irreversible.

3.2.2. Relaxation/Settling and Self Discharge

During active discharging/charging, any heat generated and not instantaneously transferred out builds up. Upon load removal, the battery settles and the heat transfers out, as the Gibbs potential proceeds to a new equilibrium. During settling, the cell voltage relaxes and the battery transfers entropy to the surroundings. To apply Equation (24) to the settling process, the external Ohmic interaction Vdq, which replaced the compositional energy changes in Equations (17) and (18), is replaced by the internal

ionic transport process energy (see Equation (19) and Equation (A8) in Appendix A). Phenomenological entropy production during settling becomes

$$\delta S\prime_{phen} = -\frac{SdT}{T} - \frac{k_B R T^2}{\eta}\frac{\partial M_C}{\partial x}dt \ln\left(\frac{m_{Li+}^{low}}{m_{Li+}^{high}}\right) \tag{28}$$

in terms of gas constant R, Li^+ concentration M_C, Boltzmann constant k_B, distance x and dynamic friction coefficient η (inverse of electrical mobility). Here, $-SdT$, positive for decreasing temperature $dT \leq 0$, represents both voltage and thermal relaxation, and the last right-hand side term represents diffusion during settling, all of which proceed spontaneously and significantly slower than the active Ohmic processes [18,19]. Equation (24) also applies to self-discharge during storage, with the external Ohmic term Vdq representing spontaneous charge leakage [2].

With voltage relaxing in opposite directions, for discharge and charge, and often canceling during cycling, entropy production during settling proceeds at the rates of spontaneous cooling and diffusion of the charge species, which, relative to the preceding and subsequent active Ohmic energy and entropy interactions (charge/discharge step), is negligible. Relaxation equilibrium is approached asymptotically, over hours to days, rendering relaxation entropy production miniscule, compared to that during charging and discharging. Additionally, many batteries continue to supply power during charge, removing settling from the cycling schedule. Considering the above, settling effects and its entropy is to be neglected.

Equations (23) and (24), over time increments dt, give rates $\dot{G} = -S\dot{T} + VI$ and $\dot{S}\prime = -\frac{S\dot{T}}{T} + \frac{VI}{T} - \frac{\dot{G}_{rev}}{T}$. Integrating from t_0 to t gives the total Gibbs energy and entropy generation

$$\Delta G = -\int_{t_0}^{t} S\dot{T}dt + \int_{t_0}^{t} VIdt \tag{29}$$

$$S\prime = -\int_{t_0}^{t} \frac{S\dot{T}}{T}dt + \int_{t_0}^{t} \frac{VI}{T}dt - \int_{t_0}^{t} \frac{\dot{G}_{rev}}{T}dt \tag{30}$$

3.3. Entropy Content S and Internal Free Energy Dissipation −SdT

In Equations (17), (21), and (22), the term $-SdT$, which represents free energy dissipated internally and not instantaneously transferred out during active work interaction, includes Ohmic dissipation and can include heat from an external source. The temperature change dT is driven by the entropy content S of the system. Resolving entropy into components, $S = S(\mu, T)$ depends on chemical potentials μ and temperature T, for a chemically reactive system. The Gibbs–Duhem equation [19,39–44]

$$SdT - \mathcal{V}dP + \sum N_k d\mu_k = 0 \tag{31}$$

at constant pressure yields

$$-SdT = \sum N_k d\mu_k \tag{32}$$

where $\sum N_k d\mu_k = Nd\mu$ for one active species (e.g., Li^+). The molar Gibbs energy at constant temperature and pressure gives the following, via Equation (17),

$$\mu = \left(\frac{\partial G}{\partial N}\right)_{T,P} \tag{33}$$

Substituting, from Equation (25), $\dot{G}_{rev} = V_{OC}I_{rev}$ and, from Equation (32), $-S\dot{T} = N\dot{\mu}$ into Equations (29) and (30) yields

$$\Delta G = \int_{t_0}^{t} N\dot{\mu}dt + \int_{t_0}^{t} VIdt \tag{34}$$

$$S\prime = \int_{t_0}^{t} \frac{N\dot{\mu}}{T}dt + \int_{t_0}^{t} \frac{VI}{T}dt - \int_{t_0}^{t} \frac{V_{OC}I_{rev}}{T}dt \tag{35}$$

Integrating Appendix A Equation (A14), Faraday's first law, yields

$$N = \frac{C}{n\prime F} \tag{36}$$

where C is the charge in the battery at time t given as

$$C(t) = C_0 \pm C_t(\Delta t) \geq 0 \tag{37}$$

C_0 is the battery's initial charge content at $t = t_0$, and

$$C_t(\Delta t) = \int_{t_0}^{t} I(t)dt \tag{38}$$

is the total charge transferred at time t. Combining Equation (20) with Equation (32) gives, in rate form,

$$-S\dot{T} = N\dot{\mu} = C\dot{V} \tag{39}$$

Substituting Equation (39) into Equations (34) and (35) yields

$$\Delta G = \int_{t_0}^{t} C\dot{V}dt + \int_{t_0}^{t} VIdt \tag{40}$$

$$S' = \int_{t_0}^{t} \frac{C\dot{V}}{T}dt + \int_{t_0}^{t} \frac{VI}{T}dt - \int_{t_0}^{t} \frac{V_{OC}I_{rev}}{T}dt \tag{41}$$

Equations (40) and (41) give Gibbs energy change and entropy production as functions of instantaneous voltage V, current I, and temperature T.

The Gibbs–Duhem constant-pressure formulation in rate form, Equation (39), shows interdependence of battery voltage and temperature—temperature rise drops voltage, and voltage drops as charge exits raises temperature (typical for active discharge), see Equations (17), (21) and (22), wherein $-SdT$ reduces the Gibbs energy for positive S and dT. Being dependent on voltage change, charge content and temperature, the batter's internal accumulation of free energy dissipation $-SdT$ is more appropriately named Electro-Chemico-Thermal (ECT) energy change, which for a reactive system depends on the number of moles, chemical potential, heat capacity, and changes in temperatures of reactive components [19,39–44]. Variables $\dot{V}$ and I, negative during discharge and positive during charge, establish similar directional signs for the Gibbs energy change and entropy generation terms. From Equation (41), the Ohmic entropy $S\prime_{\Omega} = \int \frac{VI}{T}dt$ accounts for the loss in output/input work, the reversible Gibbs entropy $S\prime_{rev} = \int \frac{V_{OC}I_{rev}}{T}dt$ measures the minimum possible loss, while the ECT entropy $S\prime_{VT} = \int \frac{C\dot{V}}{T}dt$ accounts for loss due to rise in internal entropy content and temperature, as

battery potential and charge content decrease. Similarly, from Equation (40), Ohmic work $G_\Omega = \int_{t_0}^{t} IVdt$ and ECT energy $G_{VT} = \int_{t_0}^{t} C\dot{V}dt$.

During relaxation/settling, entropy generation in Equation (41) is obtained by applying the Gibbs–Duhem formulation (Equation (31) at constant P) to Equation (28). Without any active charge transfer during settling, Equation (41) indicates that ECT entropy, the first right-hand side term representing entropy accumulation from both voltage and thermal relaxation via Equation (39), is the most significant entropy generation component. Similarly, entropy generation during battery storage, including effects of self-discharge, can be evaluated via Equation (41).

3.4. Degradation-Entropy Generation (DEG) and Capacity Fade in Batteries

In primary cells, degradation in the form of capacity loss is the difference between initial capacity at initial time t_0 and capacity at a latter time t, as the battery discharges monotonically. In secondary cells, the charge step reverses this 'loss', making the prior definition unsuitable for describing permanent loss of charge capacity. However, over time, secondary cells degrade and lose their ability to hold charge, resulting in capacity fade. This capacity fade is estimated as

$$\Delta C_{CC} = |C_1| - |C_N| \tag{42}$$

the difference between the first cycle's charge content or capacity C_1 and the Nth cycle's charge content $C_N(\Delta t)$ (capacity $C_N(\Delta t)$ can be replaced by the total charge transferred C_t, measured after a discharge step), sometimes expressed as a percentage of C_1 [15,50]. Using Coulomb/Charge Counting (subscript CC), Equation (42) requires a consistent cycling schedule and low constant discharge rate for cycles 1 and N, hence, is not applicable to irregular and inconsistent cycling schedule, with deep discharges and undercharges. Similar to Section 2.2, the above Gibbs-based formulations are combined with the DEG theorem, as follows:

- Let available battery capacity or charge content C be a DEG transformation measure and capacity fade (lost discharge/charge capacity) ΔC be the observed/measured degradation, the DEG Equation (9), with ΔC replacing Δw becomes,
$$\Delta C = \sum_i B_i S\prime_i \tag{43}$$
- From Equation (41), entropy generation $S' = S'\{V\{t\}, I\{t\}, T\{t\}\}$, suggesting via Equation (43) that $C = C\{V\{t\}, I\{t\}, T\{t\}\}$. Substituting the entropy generation terms of Equation (41) into Equation (43) gives
$$\Delta C = B_{VT} \int_{t_0}^{t} \frac{C\dot{V}}{T} dt + B_\Omega \int_{t_0}^{t} \frac{VI}{T} dt - B_G \int_{t_0}^{t} \frac{V_{OC} I_{rev}}{T} dt \tag{44}$$
- Via Equation (8), with C replacing w, DEG coefficients
$$B_{VT} = \frac{\partial C}{\partial S\prime_{VT}},\ B_\Omega = \frac{\partial C}{\partial S\prime_\Omega}, B_G = \frac{\partial C}{\partial S_{rev}} \tag{45}$$
can be evaluated via measurements, as slopes of charge C versus ECT entropy $S\prime_{VT}$, Ohmic entropy $S\prime_\Omega$ and reversible Gibbs entropy $S\prime_{rev}$. As demonstrated in Section 5, the DEG capacity fade, Equation (44), is applicable to all forms of cycling conditions.

4. Experiments

Data sets arose from degradation of four same-model Lithium-ion batteries, under inconsistent and abusive cycling. Parameters were uncontrolled—cycles discharged to different depths and recharged to

different heights, with some discharge steps extending significantly below the manufacturer-specified full-discharge depth of 2.7 V, to induce rapid degradation and severely nonlinear behavior, as this would test the robustness of the DEG degradation model. Cycle 1 discharged to 0.8 V and cycles 27 and 29 discharged down to 0.6 V. A constant current of 3 A was used for the charge steps. Figure 1 shows all four batteries during cycling. Measured cyclic data sets are in Appendix B.

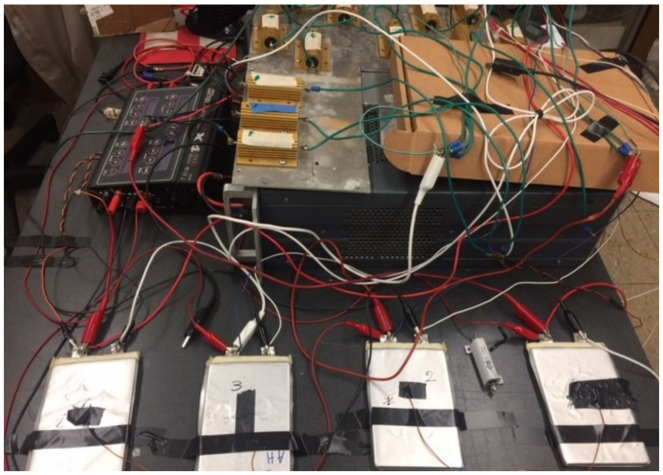

Figure 1. Photo of a portion of actual experimental set-up used in Li-ion battery measurements, showing four Li-ion batteries, a commercial charger, high-power discharge resistors, connector cables, and thermocouple wires.

4.1. Apparatus

Each setup (Figure 1) had a single-cell 3.7 V 11.5 Ah lithium-ion polymer battery with graphite anode and aluminum current-collectors, model PL-9059156, manufactured by Batteryspace; a Hitech X48 Multi-charger, powered by a DC power supply for the charge cycle; a set of Dale RH-50 1 Ω, 50 W resistors for a standardized uniform resistive load; lead wires with known gages; two duplex-insulated OMEGA TT-K-24-25 Type K thermocouples (one to measure battery temperature and the other to measure ambient temperature); a current, voltage, and resistance meter (or multimeter) (to measure pre- and post-cycling voltages and resistances), a National Instrument controller/data acquisition system NI CompactRIO with an analog input module NI 9215 (to monitor battery and resistor voltages), a digital output module NI 9401 to automate the cycling process, and a thermocouple module NI 9211 (with internal cold-junction compensation and auto-zero correction for measurement accuracy) to monitor ambient and battery temperatures.

4.2. Setup and Procedure

Figure 2 depicts the battery circuit. Monitored during cycling were battery terminal voltage V_B dependent on the switch state (set to node "c" during charge, set to node "d" during discharge and opened to measure battery open-circuit voltage V_{OC}), voltage drop across load resistor V_R, battery temperature T, and ambient temperature T_∞ near the battery. To obtain sufficient data for statistical significance and establish repeatability, four Li-ion batteries were cycled at two different unsteady discharge rates.

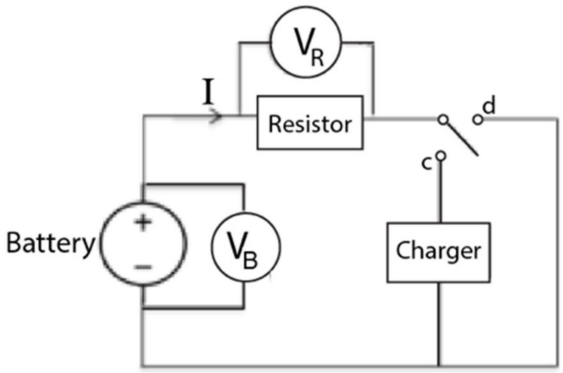

Figure 2. Discharge–charge cycle circuit for the lithium-ion batteries.

Battery tests were conducted in a well-ventilated area. All tests followed the same procedure.

4.2.1. Setup and Initial Measurements

For one battery, two 1 Ω resistors were used in parallel (actual resistance including wiring R_{load} = 0.6 Ω, measured via a multimeter); for the remaining three batteries, three 1 Ω resistors were used in parallel (R_{load} = 0.45 Ω); the sensing terminal of one thermocouple was attached to the battery surface and the ambient thermocouple was placed in air, near the battery, with the sensing terminal not in contact with any surface; the discharge–charge cycling circuit was set up with the resistor loads for cell discharging and current measurements, and a battery charger for charging (Figure 2); the initial battery voltage and temperature, and resistance of the load resistor network were measured.

4.2.2. Cycling

With the battery voltage $V_B \approx 3.7$ V and recording transient data at 0.1 Hz, the resistor network was connected to the battery to begin the discharge step; the resistors were disconnected from the battery after V_B fell to 2.7 V (full discharge) or below (over-discharge); the battery was allowed to settle for 20–25 min (for voltage and thermal relaxation); then charged at 3 A, varying the charge depths for subsequent cycles; and allowed to settle for about 30 min. This was repeated until the battery degraded, observed in one of two ways:

- the battery's capacity fell to less than two-thirds the initial capacity or
- the battery began to inflate in geometric volume (close monitoring of Li-ion batteries was required during cycling).

5. Results, Analysis, and Discussion

Monitored parameters changed with time at unsteady rates. Tables listed in this article contain data for discharge (left side of table) and charge (right side of table). Signs indicated either a parametric decrease/increase or the direction of the process; for example, ECT energy/entropy and Ohmic work/entropy are negative for discharge, and positive for charge. Path-dependent integrals were evaluated using the trapezoidal rule on data over time increment Δt. With data sampled at 0.1 Hz, $\Delta t = 10$ s. Plots show the direction of accumulation and the rates, starting with the discharge step and ending with the charge step.

Using equations for estimating charge content/transfer, Gibbs energy, and entropy (Section 3), data from the lithium-ion battery cycling experiments are presented in Tables 1 and 2, for a randomly selected battery #2. Similar trends were observed in the other same-model batteries tested. Table 1 presents the Gibbs energy-entropy data and Table 2 presents the DEG data. In both tables, column 1 contains variable N numbers the discharge–charge cycles. To add to cyclic inconsistencies, a "Half cycle" (Tables 1 and 2 and Table A1) is a charge-only cycle, which occurs when two charge steps follow a discharge step. For example, in cycle 2, the battery was fully discharged and re-charged to

about 50% nominal capacity, rested for a few hours, re-charged again in cycle 3, before discharging in cycle 4; hence, cycle 3, having no discharge step, is a half cycle. In accordance with battery industry, Ah, Wh and Wh/K are used for charge, energy, and entropy respectively (1 Ah = 3600 As = 3600 C; 1 Wh = 3600 Ws = 3600 J; 1 Wh/K = 3600 J/K), giving DEG's B coefficients units of Ah K/Wh, to differentiate them from the reciprocal of the voltage-temperature coefficient which has units of V/K (i.e., 1 Ah K/Wh = 1 K/V).

Table 1. Processed Gibbs energy and entropy parameters for Li-ion battery #2 (Discharge rate: ~5 A, Charge rate: 3 A). Cycle 6 (in bold) is used in the breakdown in this section.

	Discharge					Charge				
N	**G_Ω Wh**	**G_{VT} Wh**	**S'_Ω Wh/K**	**S'_{VT} Wh/K**	**S'_{rev} Wh/K**	**G_Ω Wh**	**G_{VT} Wh**	**S'_Ω Wh/K**	**S'_{VT} Wh/K**	**S'_{rev} Wh/K**
1	−19.93	−3.00	−0.07	−0.010	−0.11	41.40	1.00	0.14	0.003	0.13
2	−28.62	−2.22	−0.09	−0.007	−0.13	20.15	0.55	0.07	0.002	0.07
3			Half cycle			16.14	0.08	0.05	0.000	0.05
4	−32.85	−2.72	−0.11	−0.009	−0.15	15.08	0.43	0.05	0.001	0.05
5	−10.20	−0.73	−0.03	−0.002	−0.05	21.75	0.38	0.07	0.001	0.07
6	**−24.57**	**−1.64**	**−0.08**	**−0.005**	**−0.11**	**17.44**	**0.50**	**0.06**	**0.002**	**0.06**
7	−22.92	−1.73	−0.08	−0.006	−0.10	32.75	0.80	0.11	0.003	0.11
8	−33.43	−2.63	−0.11	−0.009	−0.16			Missing data		
9	−21.52	−1.39	−0.07	−0.005	−0.10	43.26	0.71	0.14	0.002	0.14
10	−30.25	−1.55	−0.10	−0.005	−0.13	6.99	0.16	0.02	0.001	0.02
11	−17.48	−1.13	−0.06	−0.004	−0.07	19.23	0.56	0.06	0.002	0.06
12	−29.00	−2.89	−0.10	−0.010	−0.13	21.49	0.62	0.07	0.002	0.07
13			Half cycle			25.34	0.87	0.08	0.003	0.08
14	−37.01	−3.11	−0.12	−0.010	−0.16	11.49	0.36	0.04	0.001	0.04
15	−20.97	−2.00	−0.07	−0.007	−0.10	18.07	0.57	0.06	0.002	0.06
16	−28.13	−1.95	−0.09	−0.006	−0.12	17.29	0.51	0.06	0.002	0.06
17	−26.99	−2.28	−0.09	−0.008	−0.12	21.45	0.65	0.07	0.002	0.07
18	−33.60	−3.65	−0.11	−0.012	−0.16	15.00	0.46	0.05	0.002	0.05
19	−21.43	−1.62	−0.07	−0.005	−0.10	17.43	0.42	0.06	0.001	0.06
20	−29.16	−3.74	−0.10	−0.012	−0.15	20.05	0.65	0.07	0.002	0.06
21	−30.39	−4.53	−0.10	−0.015	−0.16	14.90	0.24	0.05	0.001	0.05
22	−21.75	−2.56	−0.07	−0.008	−0.11	16.70	0.27	0.06	0.001	0.05
23	−25.83	−1.72	−0.09	−0.006	−0.13	17.79	0.51	0.06	0.002	0.06
24	−26.72	−2.70	−0.09	−0.009	−0.13	20.47	0.37	0.07	0.001	0.07
25	−11.73	−0.31	−0.04	−0.001	−0.05	50.85	0.56	0.17	0.002	0.16
26	−40.64	−5.32	−0.13	−0.017	−0.21	17.52	0.50	0.06	0.002	0.06
27	−25.68	−5.24	−0.08	−0.017	−0.18	33.06	0.51	0.11	0.002	0.11
28			Half cycle			21.13	0.26	0.07	0.001	0.07
29	−18.09	−3.55	−0.06	−0.012	−0.14	37.18	0.49	0.12	0.002	0.12
30	−11.39	−1.53	−0.04	−0.005	−0.07	40.44	0.44	0.13	0.001	0.13
31	−17.74	−2.32	−0.06	−0.008	−0.09	39.20	0.54	0.13	0.002	0.13
32	−9.67	−1.21	−0.03	−0.004	−0.06	19.96	0.74	0.07	0.002	0.07
		SUMMARY/TOTAL								
			−2.34	−0.234	−3.47			2.43	0.053	2.39

Table 2. Processed Degradation-Entropy Generation (DEG) and Coulomb-Counted capacity fade parameters for Li-ion battery #2 (Discharge rate: ~5 A, Charge rate: 3 A). Cycle 6 (in bold) is used in the Capacity Fade discussion.

	Discharge					Charge			
N	C_{phen} **Ah**	C_{rev} **Ah**	ΔC_{DEG} **Ah**	C_{CC} **Ah**	ΔC_{CC} **Ah**	C_{phen} **Ah**	C_{rev} **Ah**	ΔC_{DEG} **Ah**	C_{CC} **Ah**
1	−6.5	−7.6	1.1	−6.1	0.0	10.7	10.1	0.6	10.5
2	−7.7	−9.3	1.6	−8.4	−2.3	5.3	5.0	0.3	5.2
3			Half cycle			3.8	3.8	0.0	4.0
4	−9.4	−10.4	1.0	−9.5	−3.4	3.8	3.7	0.1	3.8
5	−2.5	−3.3	0.8	−3.0	3.1	5.3	5.2	0.1	5.4
6	**−6.7**	**−8.0**	**1.3**	**−7.2**	**−1.1**	**4.6**	**4.3**	**0.3**	**4.4**
7	−6.8	−7.3	0.5	−6.7	−0.6	8.4	7.9	0.5	8.2
8	−9.4	−10.6	1.2	−9.7	−3.6		Missing data		
9	−5.9	−7.1	1.2	−6.4	−0.3	10.6	10.4	0.2	10.8
10	−8.2	−9.2	1.0	−8.7	−2.6	1.5	1.5	0.0	1.6
11	−5.0	−5.7	0.7	−5.2	0.9	4.6	4.6	0.0	4.8
12	−8.8	−9.5	0.7	−8.5	−2.4	5.3	5.2	0.1	5.4
13			Half cycle			6.1	6.1	0.0	6.3
14	−10.3	−11.0	0.7	−10.5	−4.4	3.0	2.9	0.1	3.0
15	−6.2	−6.9	0.7	−6.2	−0.1	4.6	4.4	0.2	4.6
16	−7.6	−9.0	1.4	−8.3	−2.2	4.6	4.2	0.4	4.4
17	−7.8	−8.7	0.9	−8.0	−1.9	5.3	5.2	0.1	5.4
18	−9.8	−11.1	1.3	−10.0	−3.9	3.8	3.7	0.1	3.8
19	−5.9	−7.1	1.2	−6.4	−0.3	4.6	4.3	0.3	4.4
20	−9.0	−10.4	1.4	−9.0	−2.9	5.3	4.9	0.4	5.1
21	−9.4	−11.2	1.8	−9.5	−3.4	3.8	3.7	0.1	3.8
22	−6.3	−7.8	1.5	−6.8	−0.7	4.6	4.1	0.5	4.2
23	−7.6	−9.0	1.4	−7.9	−1.8	4.6	4.3	0.3	4.5
24	−7.9	−9.4	1.5	−8.2	−2.1	5.3	5.0	0.3	5.2
25	−3.2	−3.5	0.3	−3.4	2.8	12.9	12.0	0.9	12.5
26	−11.9	−14.0	2.1	−12.4	−6.3	4.6	4.3	0.3	4.4
27	−8.0	−12.7	4.7	−8.8	−2.7	8.4	8.0	0.4	8.3
28			Half cycle			5.3	5.1	0.2	5.3
29	−6.0	−9.9	3.9	−6.4	−0.3	9.1	8.9	0.2	9.2
30	−3.6	−4.7	1.1	−3.8	2.4	9.8	9.6	0.2	10.0
31	−5.5	−6.8	1.3	−5.8	0.3	9.9	9.3	0.6	9.6
32	−2.8	−3.9	1.1	−3.2	2.9	5.3	4.9	0.4	5.1
			SUMMARY/TOTAL						
	−205.7	−245.0	39.3	−213.8		185.0	176.8	8.2	183.2

Figure 3 plots measured discharge and charge current I, battery voltage V, and temperature T versus time, during cycle 6. With a constant resistive load R_{load}, V and I trend similarly during discharge. In Figure 3, battery temperature rose during discharge but remained relatively steady during charge, trending with ambient temperature.

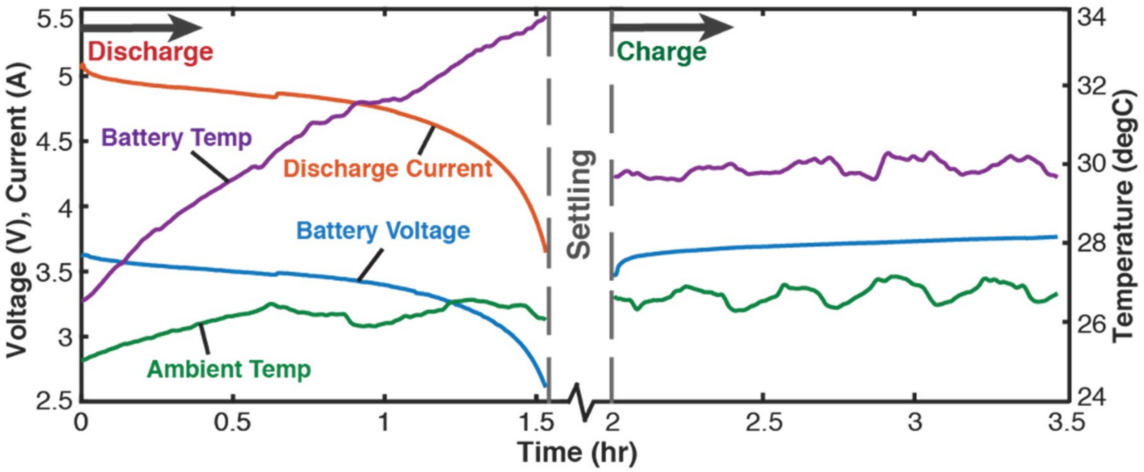

Figure 3. Monitored parameters during cycling (cycle 6 data) showing 1.5 h discharge starting at ~5 A, followed by 0.4 h settling and 1.5 h constant-current charge at 3 A.

5.1. Gibbs Energy and Entropy Components

Columns 2 and 7 of Table 1 list the discharge and charge Ohmic work G_Ω, and columns 3 and 8 show the ECT energy G_{VT}. Figure 4 plots Ohmic S'_Ω (columns 4 and 9 of Table 1), ECT S'_{VT} (columns 5 and 10) and reversible Gibbs S'_{rev} (columns 6, 11) entropies, versus charge transferred. Continuous curves represent discharge and dashed curves represent charge profiles, both processes proceeding in opposite directions. Measured charge transfer (Figure 4) appears linear vs. Ohmic entropy S'_Ω (blue plots) and curvilinear vs. ECT entropy S'_{VT} (red plots). Voltage relaxation after discharge typically reduces charge S'_{VT}. In other words, when the external load is disconnected from the battery, the battery's potential V immediately rises, indicating voltage elasticity and causing the voltage change during active charge to be less than that during discharge. This contributes to higher Coulombic efficiency of the charge step in battery cycling, and verifies that charging is more thermodynamically reversible than discharging, and hence generates less entropy. Note that a reversible (ideal) step is one that proceeds at a constant current and voltage. Figure 4 shows Ohmic entropy to be several times that of the ECT entropy, seemingly justifying the latter's absence in many battery analyses. However, the significance of the ECT entropy is underscored by the need to avoid overdischarging and overcharging, and keep batteries cool during operation, for better and longer performance.

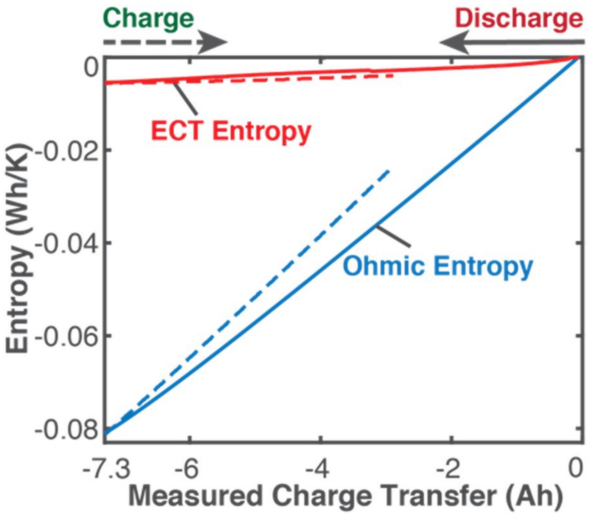

Figure 4. Phenomenological entropy components (Ohmic and Electro-Chemico-Thermal (ECT)) vs. measured charge transfer during discharge (solid curves) and charge (dashed curves).

Figure 5 plots rates of entropy generation components versus time. Ohmic entropy rate starts relatively high and decreases during discharge; vice versa during charge. ECT entropy generation rate fluctuates significantly with a slight overall change, during both discharge and charge. These fluctuations have higher amplitudes during discharge than charge. Rate of reversible Gibbs entropy, steady for both discharge and charge, is higher for discharge via higher discharge rate.

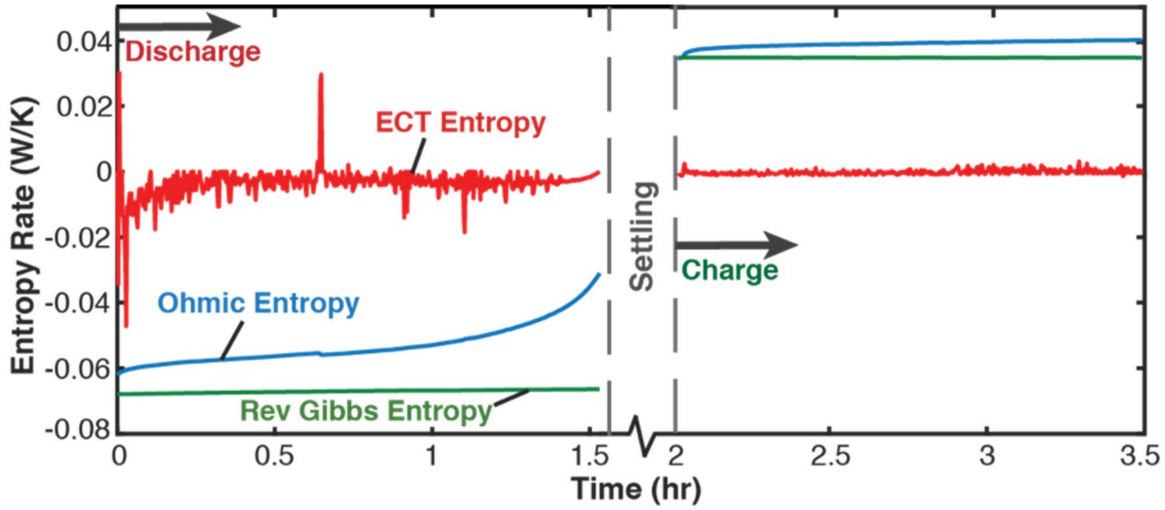

Figure 5. Entropy generation component rates (Ohmic, ECT, and reversible Gibbs) over time, during discharge and charge.

Figure 6 plots the primary components of entropy generation—phenomenological entropy $S\prime_{phen}$ (purple plots) and reversible entropy $S\prime_{rev}$ (green plots)—during discharge and charge steps of cycle 6. The region between $S\prime_{rev}$ and $S\prime_{phen}$ curves represents the entropy generated $S\prime$. During discharge and charge, $S\prime_{rev} < S\prime_{phen}$ as anticipated by Equation (26), in accordance with the second law. Entropy generation is significantly higher during discharge with higher values of current and deep discharge.

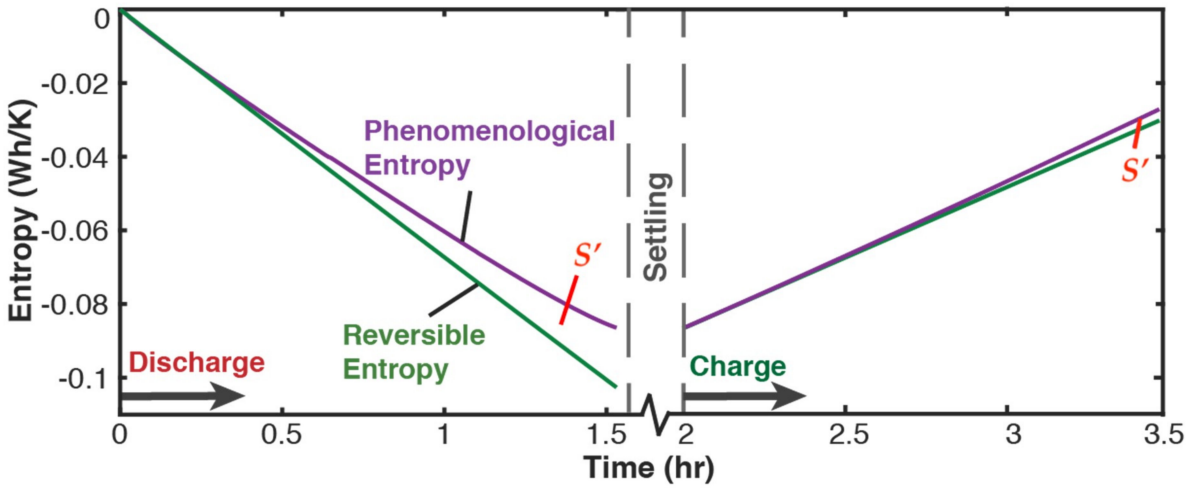

Figure 6. Entropy generation $S\prime$ and components during cycle 6's discharge and charge steps. The region between reversible entropy and phenomenological entropy curves represents entropy generation.

Similar results were observed for all cycles and all four batteries.

The final 'Summary/Total' row of Table 1 shows that the total Ohmic entropy $S\prime_{\Omega}$ is about 10 times the total ECT entropy $S\prime_{VT}$ for all the discharge steps combined, whereas all the charge steps collectively accumulated ratio $S\prime_{\Omega}$:$S\prime_{VT}$ at the much more thermodynamically reversible 46:1. Discharge $S\prime_{VT}$ is

4.4 times the charge $S\prime_{VT}$ (via a higher entropy generation rate from discharge rate >> charge rate and deep discharging), while charge $S\prime_{\Omega}$ is higher than the discharge $S\prime_{\Omega}$ (via the overall charge duration >> discharge duration). Total reversible entropy $S\prime_{rev}$ is less than the total phenomenological entropy for both discharge and charge, in accordance with thermodynamic formulations.

5.2. DEG—Capacity Versus Entropy

By associating data for entropies and battery charge at various time instants, Figure 7 plots charge C (measured via integration of battery current) versus accumulated entropy components $S\prime_{\Omega}$ (Ohmic) and $S\prime_{VT}$ (ECT). Figure 7a shows the three-dimensional plots for discharge, curve 'D' on the red plane, and charge, curve 'C' on the green plane. End views in Figure 7b show a near perfect coincidence of all data points onto these planes. A goodness of fit $R^2 \approx 1$ was obtained for all measured data, for all cycles of all four batteries tested. The near perfect coincidences onto 2D planes suggest a linear dependence of battery charge on both Ohmic and ECT entropies at every instant of the discharge/charge process, consistent with the predicted linearity of Equation (43). The dimensions of the horizontal axes and their maximum values are determined by the accumulation of the entropy generation components at the end of the discharge/charge step.

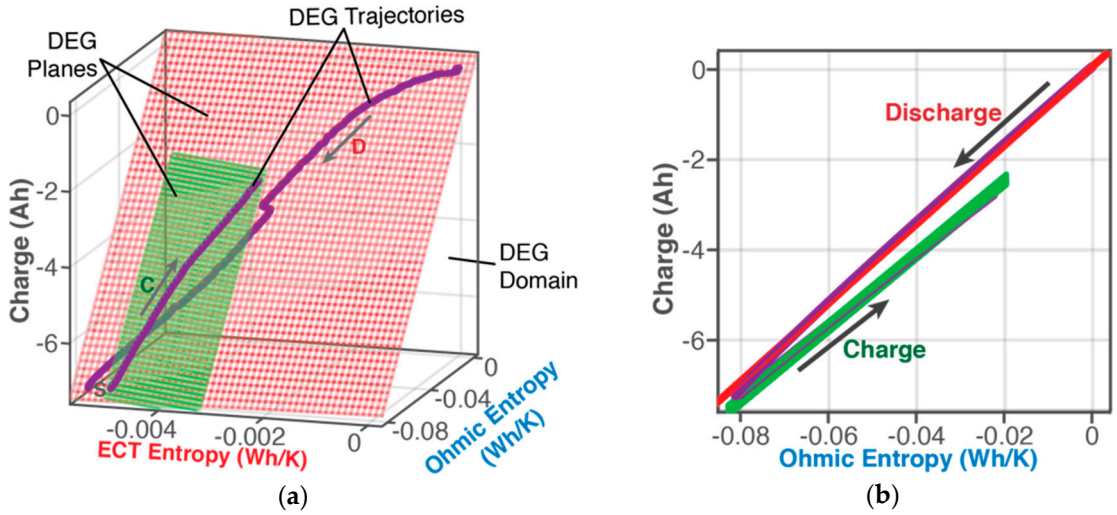

Figure 7. (**a**) 3D plots and linear surface fits of Charge (vertical axes) vs. Ohmic and ECT entropies (horizontal axes) during discharge (red plane, curve 'D' starts from upper right corner) and charge (green plane, curve 'C' starts from lower left corner) steps of cycle 6, indicating a linear dependence on two active processes. (**b**) The end projection of the planes and curves of (**a**), and a visual of the goodness of fit. Axes are not to scale.

In Figure 7, the measured data points for both discharge and charge form distinct paths—-deemed Degradation-Entropy Generation (DEG) trajectories which lie on (coincide with) planar surface(s), deemed DEG plane(s)/surface(s). The 3D space of the DEG surface(s), the battery's DEG domain, appears to characterize the allowable regime in which the battery can operate.

Degradation Coefficients: The red and green DEG planes in Figure 7 have orientations in the 3D DEG domain that can be specified in terms of partial derivatives of charge with respect to Ohmic and ECT entropies respectively. Via Equation (45), these orientations (or partial derivatives) define the Ohmic and ECT degradation coefficients B_{Ω} and B_{VT}. Data from a reference cycle (cycle 1 in this study) was used to obtain the battery's characteristic DEG coefficients and predict the rest of the battery's operational life. From cycle 1 data, $B_{\Omega} = 76.6$ Ah K/Wh and $B_{VT} = 113$ Ah K/Wh for discharge, and for charge, $B_{\Omega} = 75.5$ Ah K/Wh and $B_{VT} = 28.3$ Ah K/Wh.

5.2.1. Phenomenological Charge, Measured Charge, and Reversible Charge

The Carnot limitation—a corollary constraint of the second law which governs availability of a system's energy for work—was expressed by Burghardt [45] for a heat source as

$$Energy\ added\ =\ Available\ energy\ +\ Unavailable\ energy \tag{46}$$

Defining phenomenological charge transfer C_{phen}, the battery's actual physically observable path which can be correlated directly with phenomenological entropy via the first two right-hand side terms in Equation (41) as

$$C_{phen} = C_t + \Delta C_{phen} = B_{VT}\int_{t_0}^{t}\frac{C\dot{V}}{T}dt + B_{\Omega}\int_{t_0}^{t}\frac{VI}{T}dt \tag{47}$$

where the phenomenological capacity fade ΔC_{phen}, a portion of C_{phen} not available for external/boundary work during cycling due to instantaneous dissipation from battery heating and loss of charge and potential, is the difference between the phenomenological charge transfer C_{phen} and measured charge transfer $C_t = \int_{t_0}^{t} I(t)dt$. Similarly, defining reversible charge transfer C_{rev} that establishes the battery's ideal path and correlates with reversible entropy, the last term of Equation (41),

$$C_{rev} = C_t + \Delta C_{rev} = B_G\int_{t_0}^{t}\frac{V_{OC}I_{rev}}{T}dt \tag{48}$$

where reversible charge fade ΔC_{rev} is the difference between reversible (ideal) charge transfer

$$C_{rev} = \int_{t_0}^{t} I_{rev}dt = I_{rev}\Delta t \tag{49}$$

and measured charge transfer C_t (or accumulated discharge/charge). Here C_{rev} is maximum during discharge (maximum discharge capacity) and minimum during charge (minimum charge capacity); ΔC_{rev} represents the portion of C_{rev} unavailable due to previous permanent degradation and instantaneous dissipation; and I_{rev} is the constant reversible current, maximum during discharge and minimum during charge.

Following Equation (26), the difference between Equations (47) and (48) derives Equation (44), the DEG capacity fade model, which quantifies actual capacity fade from degradation

$$\Delta C_{DEG}(\Delta t) = C_{phen} - C_{rev} = B_{VT}\int_{t_0}^{t}\frac{C\dot{V}}{T}dt + B_{\Omega}\int_{t_0}^{t}\frac{VI}{T}dt - B_G\int_{t_0}^{t}\frac{V_{OC}I_{rev}}{T}dt \tag{50}$$

as the difference between phenomenological and reversible charge transfer components. Inspection of Equations (48) and (49) indicates that $B_G = \frac{dC_{rev}}{dS_{rev}} = \frac{T}{V_{OC}}$. Substituting $I_{rev}\Delta t$ (from Equation (49) with I_{rev} constant) for the last term in Equation (50) gives

$$\Delta C_{DEG}(\Delta t) = B_{VT}\int_{t_0}^{t}\frac{C\dot{V}}{T}dt + B_{\Omega}\int_{t_0}^{t}\frac{VI}{T}dt - I_{rev}\Delta t \tag{51}$$

While C_t and C_{rev} are determined from currents I and I_{rev}, and C_{phen} is not directly measurable. This makes Equation (51), the simplified form of the DEG model in Equation (44)—which requires only measurements of V, I and T—convenient for instantaneous evaluation of operational capacity fade, irrespective of discharge rate, depth of discharge, and cycling inconsistencies.

During discharge, C_{rev} in Equations (48) and (49) represents the overall maximum charge available in the battery, only obtained from new batteries (at $t = t_0, C_{rev} = C_{phen}$) or if the battery operates as a perfect energy source or sink (wherein no output or input power converts to heat or degrades the battery). As the battery ages, C_{phen} diminishes (i.e., at $t > t_0$, $|C_{phen}| < |C_{rev}|$). As degradation continues, the amount of energy required to restore the battery's original charged state increases. Hence, during charge, C_{rev} is the overall minimum charge required to restore the battery to its initial state, realizable in new batteries (i.e., at $t = t_0, C_{rev} = C_{phen}$), while C_{phen} is the actual increasing charge from the external charger, required to restore the battery to its original state (i.e., at $t > t_0, C_{phen} > C_{rev}$). This implies $\Delta C > 0$ consistently represents the capacity fade during both discharge and charge in accordance with positive entropy generation $S' > 0$, Equation (26).

Table 2 presents the components of the DEG capacity fade ΔC_{DEG} and Coulomb-Counted capacity fade ΔC_{CC} for the discharge and charge steps of all 32 cycles monitored.

5.2.2. Evaluating Capacity Fade—Battery Cycle Life Model

Cyclic values of DEG capacity fade ΔC_{DEG} and Coulomb-Counted capacity fade ΔC_{CC} presented in Table 2 for cycles 1 to 32, were obtained as follows:

1. Evaluate phenomenological charge C_{phen} in Table 2, columns 2 (discharge) and 7 (charge), from Equation (47), by combining reference DEG coefficients with each cycle's phenomenological entropy components S'_{Ω} and S'_{VT} given in Table 1. For example, the discharge step of cycle 6, row 6 of Table 1, has $S'_{\Omega} = -0.08$ Wh/K, and $S'_{\mathrm{VT}} = -0.005$ Wh/K. When combined with $B_{\Omega} = 76.6$ Ah K/Wh and $B_{VT} = 113$ Ah K/Wh from cycle 1, Equation (47) gives C_{phen} = (76.6 × −0.08) + (113 × −0.005) = −6.7 Ah.
2. Evaluate reversible charge C_{rev} (Table 2, columns 3 and 8) from Equation (49). For example, the cycle 1 starting current $I_1(t_1) = -5.2$ A gives the cycle 6 discharge $I_{rev} = -5.2$ A which, with the cycle 6 discharge duration Δt = 1.53 h (Table A1 in Appendix B), gives C_{rev} = −5.2 × 1.53= −8.0 Ah.
3. Evaluate DEG capacity fade (Table 2, columns 4 and 9) from Equation (51), $\Delta C_{DEG} = C_{phen} - C_{rev}$. For cycle 6 discharge, $\Delta C_{\mathrm{DEG}} = -6.7 - (-8.0) = 1.3$ Ah. Similarly, for cycle 6 charge, $\Delta C_{\mathrm{DEG}} =$ 0.3 Ah.
4. Evaluate cyclic Coulomb-Counted charge transfer (Table 2, columns 5 and 10), $C_{\mathrm{CC}} = \int_{t_0}^{t} I(t)\mathrm{d}t$ where *I(t)* is instantaneously measured unsteady current. For cycle 6 discharge and charge, row 6 of Table 2, C_{CC}= −7.2 Ah and 4.4 Ah respectively.
5. Evaluate Coulomb-Counted capacity fade (Table 2, column 6) from Equation (42), $\Delta C_{CC} = |C_1| - |C_{CC}|$, where $C_1 = -6.1$ Ah is Coulomb-Counted charge transfer during cycle 1 discharge. For cycle 6, ΔC_{CC} = |−6.1| − |−7.2| = −1.1 Ah.

From the above procedure, substituting cycle 1 discharge's pair of DEG coefficients (given in Section 4.2) and reversible current—obtained as cycle 1's starting discharge current $I_{rev} = I_1(t_1)$—into Equation (51), the discharge (subscript *d*) capacity fade model for the Li-ion battery used in this study becomes,

$$\Delta C_{DEG}|_d = 113 S'_{VT} + 76.6 S'_{\Omega} - I_1(t_1)\Delta t \tag{52}$$

Similarly, for the charge steps, with $B_{\Omega} = 75.5$ Ah K/Wh, $B_{VT} = 28.3$ Ah K/Wh and $I_{rev} = I_1(t_n)$, obtained at the end of cycle 1's charge step t_n, the battery's charge *c* capacity fade model is

$$\Delta C_{DEG}|_c = 28.3 S'_{VT} + 75.5 S'_{\Omega} - I_1(t_n)\Delta t \tag{53}$$

The battery cycle life models, Equations (52) and (53), are in the form of first-order partial differential equations with constant coefficients. The slight difference in discharge and charge B_{Ω} values is primarily attributed to the difference in discharge and charge currents, while the significant difference in discharge and charge B_{VT} is due to the different instantaneous responses to the different

operating conditions. Figure 8, plots of all 32 cyclic phenomenological charges vs. cyclic Ohmic and ECT entropies, shows each discharge and charge step's characteristic operational conditions (depth of discharge, etc.) and response to those conditions, via the scatter in the cyclic C_{phen} data. However, as predicted by Equations (52) and (53), and more easily observed in Figure 8b, all cyclic responses by the battery to the given operational conditions lay on the same DEG planes, giving a consistent prediction of the battery's cycle life.

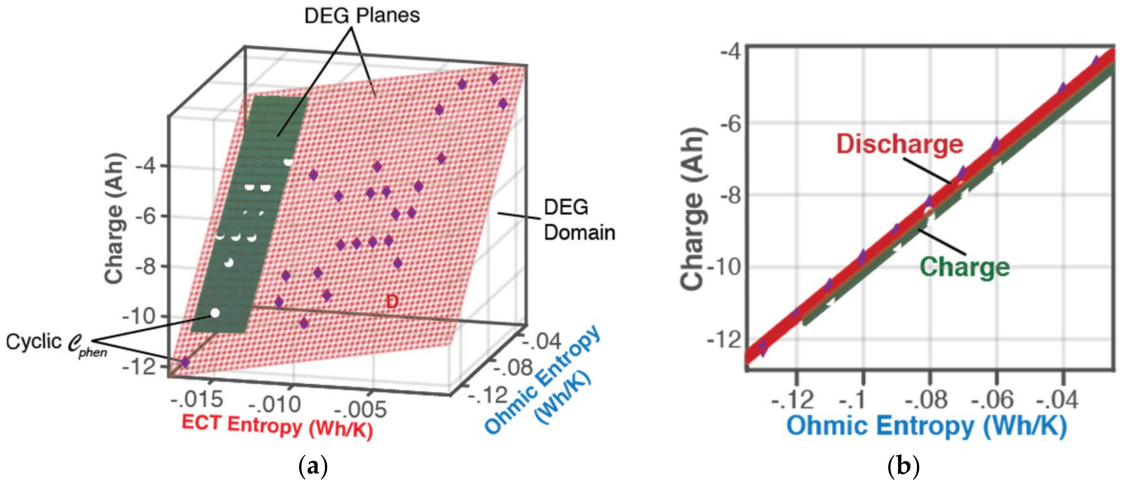

Figure 8. (**a**) 3D scatter of cyclic phenomenological C_{phen} (vertical axis) vs. Ohmic and ECT entropies (horizontal axes) for all discharge steps (purple dots on red plane) and charge steps (white dots on green plane) shows that all 32 cycles lay on cycle 1's DEG planes, a visual of Equations (52) and (53); (**b**) end projection of (**a**) shows a linear relationship. Axes are not to scale.

Cycle 1 characterized the battery via the B coefficients and Equations (52) and (53), or Equation (44). Data from subsequent cycles were used to monitor the battery's degradation with cycling. Tables 1 and 2 show that steps with high electro-chemico-thermal (ECT) entropy (relative to Ohmic entropy) had high DEG capacity fade ΔC_{DEG} (discharge steps 27 and 29, both of which had the lowest discharge cut-off voltage of 0.6 V, indicating the deepest discharge—see Table A1 in Appendix B). With each charge step proceeding at the steady rate of 3 A, the charge entropy generation was determined primarily by the duration of charge, hence steps with more accumulated charge tended to have higher entropy generation and hence, higher charge capacity fade (charge steps 1, 7, 25, 31).

Due to the severely inconsistent cycling of varying discharge and charge depths, Coulomb-Counted capacity fade ΔC_{CC} (Equation (42)) which depends only on current, was not applicable to the measured data sets. Discharge values are presented in Table 2, column 6, only for comparison to the DEG capacity fade ΔC_{DEG}. The effects of the irregular discharge durations are easily observed in ΔC_{CC} values in Table 2, with most cycles falsely indicating improvement (increased charge capacity) over cycle 1, even with the insufficient recharge in the preceding charge steps and low discharge depths—down to < 1 V, in several cases. The DEG capacity fade is a function of each cycle's entropy generation, which is in turn a function of each cycle's phenomenological state variables (V, I and T). Table 2's 'Summary/Total' row shows the total DEG discharge capacity fade of 39.3 Ah, relative to an ideal/reversible total of 245 Ah discharge obtained from the battery (16.0%), and charge capacity fade of 8.2 Ah relative to a total of 176.8 Ah charge supplied to the battery (4.6%), suggesting that most of the battery's loss of usable charge-holding capacity occurred during discharge (particularly deep discharge), in accordance with experience. Based on the battery's nominal capacity rating of 11.5 Ah, the battery's nominal DEG capacity fade was estimated via

$$\Delta C_{DEG}(\Delta t) = \left(\frac{C_{phen} - C_{rev}}{C_{rev}}\right) C_{norm} \tag{54}$$

as (0.16 × 11.5=) 1.83 Ah discharge fade and (0.046 × 11.5=) 0.53 Ah charge fade.

Figure 9 plots capacity fade components—measured charge C_t (blue plot), phenomenological charge C_{phen} (purple plot), and reversible charge C_{rev} (green plot)—during discharge and charge steps of cycle 6, with capacity fade ΔC as the region between C_{rev} and C_{phen} curves. During both discharge and charge, $C_{rev} < C_{phen}$; note that using the magnitude only, during discharge, $|C_{phen}| < |C_{rev}|$. These consistent trends were anticipated by formulations in accordance with the second law, see previous sections. As with entropy generation in Figure 6, discharge capacity fade was significantly higher than the charge capacity fade, due to a faster and deeper discharge than charge. With relatively low ECT entropy, $C_{phen} \approx C_t$ (Figure 9).

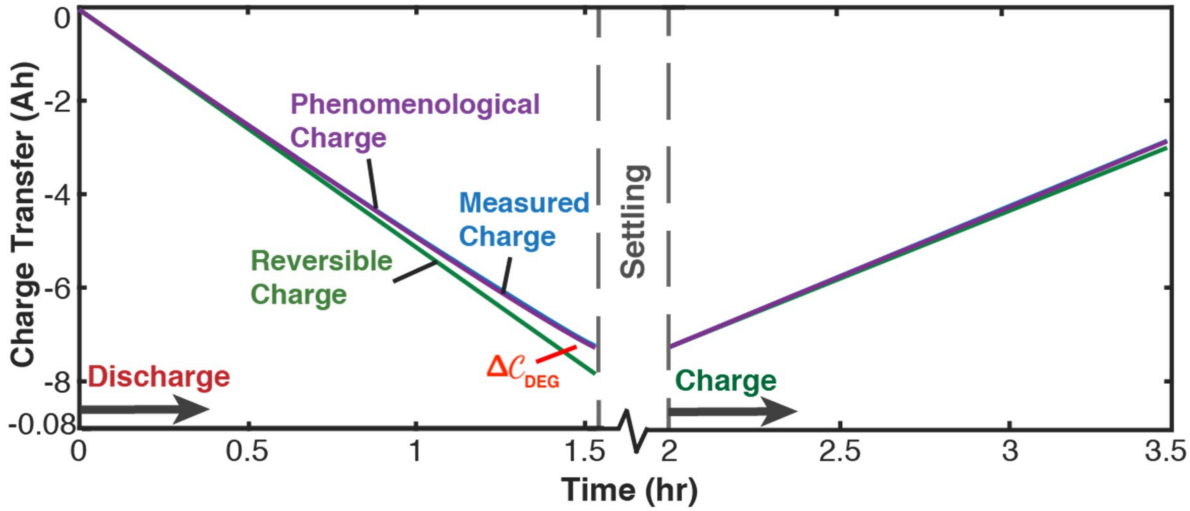

Figure 9. Capacity fade and components for cycle 6's discharge and charge. The region between reversible and phenomenological charge transfer curves is capacity fade ΔC.

6. Discussion

Prigogine [42] introduced a universally non-positive (for macroscopic systems undergoing spontaneous processes), interaction-specific "local potential", which is analogous to the ECT entropy introduced in this study. This article derived and experimentally verified a universally consistent system-based, time-dependent entropy generation. It was shown that,

- phenomenological entropy generation S'_{phen} is the sum of Ohmic entropy S'_{Ω} and electro-chemico-thermal ECT entropy S'_{VT};
- entropy generation is the difference between phenomenological S'_{phen} and reversible S'_{rev} Gibbs entropies, at every instant;
- entropy generation is always non-negative, in accordance with the second law, whereas components S'_{phen} and S'_{rev} are directional—positive during charge and negative during discharge. This implies $|S'_{phen}| \geq |S'_{rev}|$ during charge and $|S'_{phen}| \leq |S'_{rev}|$ during discharge, in accordance with experience and thermodynamic laws. This article demonstrated the significance of the previously neglected reversible S'_{rev} and ECT S'_{VT} entropies in evaluating entropy generation in batteries.

6.1. Features of the DEG Theorem and Coefficients

The DEG methods can accurately describe the battery's charge levels (or state of charge SOC) within a discharge–charge cycle and the capacity fade over multiple discharge–charge cycles, using entropy generation components. DEG coefficients relate operational capacity fade to entropy generation in a rechargeable battery at any point in the battery's life, by quantifying the dissipative processes' individual contributions to the battery's degradation. Ohmic coefficient $B_{\Omega} > 0$ via Equation (44), where phenomenological entropy components and charge transfer are negative during discharge and

positive during charge, while ECT coefficient B_{VT} has a varying sign. This is implied in Equation (47), rewritten as

$$B_{VT} = \frac{1}{S\prime_{VT}}\left(C_{phen} - B_{\Omega}S\prime_{\Omega}\right) \tag{55}$$

where both C_{phen} and $B_{\Omega}S\prime_{\Omega}$ are negative during discharge and positive during charge.

6.1.1. DEG Trajectories, Surfaces, and Domains

The DEG theorem converts degradation failure modeling and concomitant design into a multi-dimensional geometry problem, as Figures 7 and 8 suggest. The volume spanned by entropy trajectories defines the operating and aging region, as well as the consistent parameters for identifying desired characteristics from batteries of all configurations. Phenomenological entropy components serve as axes in the multi-dimensional space of C versus $S\prime_i$, where i numbers the active processes. DEG trajectories characterize the discharge–charge cycle conditions; inclination and location of DEG surfaces appear to characterize a battery's discharge/charge rates; and the DEG domain (here Charge versus Ohmic and ECT Entropies) seems to characterize the battery life, for all cycles and all rates. A battery having a domain with large accumulated charge dimension and small ECT entropy dimension (relative to Ohmic entropy dimension) delivers power more efficiently.

7. Summary and Conclusions

This study applied irreversible thermodynamics to instantaneous characterization of lithium-ion battery degradation. The DEG theorem was successfully applied to nonlinear lithium-ion battery cycling, using non-intrusive measurements of temperature, voltage, and current. Detailed thermodynamic breakdown of the active electrochemical processes in lithium-ion batteries during cycling was presented, and the kinetics (see Appendix A) were represented with universally consistent and easily measurable battery operational parameters to determine the components of energy change and entropy generation. Via entropy generation evaluation, battery capacity fade model was formulated from the DEG theorem and experimentally verified, for four same-model lithium-ion batteries. The electro-chemico-thermal ECT entropy was introduced and its contribution to capacity fade was demonstrated. In the formulations of this article, operational capacity fade depended on the usual phenomenological variables used by the battery industry, but through the entropy generated by the underlying dissipative processes. A thermodynamic potential—Gibbs free energy—replaced the steady state assumptions of previous DEG applications, and employed the instantaneous applicability of the first and second laws of thermodynamics. The DEG methodology could directly compare the same-model and different-model lithium-ion batteries, as well as technologies, designs, and materials used in manufacturing the battery.

Author Contributions: Conceptualization, J.A.O. and M.D.B.; Data curation, J.A.O.; Formal analysis, J.A.O.; Funding acquisition, M.D.B.; Investigation, J.A.O.; Methodology, J.A.O. and Michael Bryant; Resources, J.A.O. and M.D.B.; Software, J.A.O.; Validation, J.A.O.; Visualization, J.A.O.; Writing—original draft, J.A.O.; Writing—review & editing, J.A.O. and M.D.B..

Acknowledgments: The authors thank the University of Texas at Austin Mechanical Engineering Department's Fall 2015 semester Mechatronics I students for their assistance in the battery measurements.

Conflicts of Interest: The authors declare no conflict of interest.

Abbreviations

Nomenclature	**Name**	**Unit**
A	chemical affinity	J/mol
B	DEG coefficient	Ah K/Wh
C	charge, charge transfer or capacity	Ah
ΔC	charge or capacity fade	Ah
F	Faraday's constant	C/mol
G	Gibbs energy	Wh
I	discharge/charge current or rate	A
k_B	Boltzmann constant	J/K
m	mass	kg
n'	number of charge species	
N	cycle number	Kg/mol
N, N_k	number of moles of substance	mol
p	dissipative process energy	J
P	pressure	Pa
q	charge	Ah
Q	heat	J
R	gas constant	J/mol·K
S	entropy or entropy content	Wh/K
S'	entropy generation or production	Wh/K
t	time	sec
T	temperature	degC or K
U	internal energy	J
V	voltage	V
$\mathcal{V}$	volume	m^3
w	degradation measure	
W	work	J
Symbols		
μ	chemical potential	
ζ	phenomenological variable	
Subscripts & acronyms		
Ω	Ohmic	
0	initial	
c	charge	
d	discharge	
ECT, VT	Electro-Chemico-Thermal	
t	time	
rev	reversible	
irr	irreversible	
phen	phenomenological	
CC	Coulomb-Counted	
DEG	Degradation-Entropy Generation	

Appendix A

A.1. Electrochemical Kinetics

Reversible reduction and oxidation reactions at the cathode and anode, and transport of ions through the electrolyte underlie lithium-ion battery operation. In Equation (18), these kinetics are embedded in the compositional change term $\sum \mu_k dN_k$. This section formulates equations governing electrochemical kinetics of charge formation (ionization reaction) and charge transport [19,38,42].

A.1.1. Charge Intercalation (Absorption) and Deintercalation (Release)

For the reversible chemical reactions at the cathode and anode expressed respectively in Equations (1) and (2), changes in mole numbers of active species can be related stoichiometrically, via

$$\begin{aligned} \frac{dN_{Li_{1-x}MO_2}}{-1} = \frac{dN_{Li^+}}{-x} = \frac{dN_{e^-}}{-x} = \frac{dN_{LiMO_2}}{1} = d\xi_{ca} \\ \frac{dN_{Li_xC_6}}{-1} = \frac{dN_{C_6}}{1} = \frac{dN_{Li^+}}{x} = \frac{dN_{e^-}}{x} = d\xi_{an} \end{aligned} \tag{A1}$$

where $d\xi_{ca} = d\xi_{an} = d\xi$ is the reaction extent. Subscripts *ca* and *an* represent the cathode and anode respectively. Combining the above renders an equation involving de Donder's reaction affinity A which drives the reaction [1], that is

$$\sum \mu\prime_k dN\prime_k = Ad\xi \tag{A2}$$

A.1.2. Reaction Rates

Combining forward reaction rate $K_f = l_f a_{Li_{1-x}MO_2} a_{Li_xC_6}$ applicable to battery charging, reverse reaction rate $K_r = l_r a_{LiMO_2} a_{C_6}$ applicable to battery discharging, affinity $A = RT\ln\left(\frac{K_f}{K_r}\right)$ [19], and reaction extent $d\xi = (K_f - K_r)$, gives

$$\sum \mu\prime_k dN\prime_k = RT(K_f - K_r)\ln\left(\frac{K_f}{K_r}\right) \tag{A3}$$

Here l_f, l_r are the reaction rate constants, often evaluated from the Arrhenius equation $l = l_0 e^{-E_A/RT}$, a represents the activity of a species given by the subscript, and R is the gas constant.

A.1.3. Charge Transport

In a typical reaction, consumption of an active species slows the reaction, hence the chemical potential depends on the amount of the species. Similarly, in a continuous system containing two regions of an active species, diffusion will occur if the amount of the species in one region (and consequently the region's chemical potential) is lower than in the other region. Diffusion tends to equalize the chemical potentials of both regions, hence the thermodynamic force that drives this flow, the diffusion affinity $\left(\mu_{high} - \mu_{low}\right)$, is the difference in species chemical potentials in regions inside the system [19], e.g., battery. In terms of the reaction extent, diffusion work is given as $\left(\mu_{high} - \mu_{low}\right)d\xi$. As done for chemical affinity (using the reaction rates) above,

$$\left(\mu_{high} - \mu_{low}\right) = RT\ln\left(\frac{m^{low}_{Li+}}{m^{high}_{Li+}}\right) \tag{A4}$$

expressed in terms of molalities $m^{high}_{Li+}, m^{low}_{Li+}$ (mol/kg) of Li^+ in both regions. Activity a^{low}_k could also be used for convenience.

Fick's laws of diffusion and ion conservation [1,19] govern the diffusion work in the presence of concentration gradients. The diffusion current $\dot{N}^d{}_k$ (x_k,t) (mol/cm^2·s) in terms of Li^+ concentration M_c (x_k,t) (mol/cm^3) and the diffusion coefficient D (cm^2/s) can be written as

$$\dot{N}^d{}_k = -D\frac{\partial M_C}{\partial x_k} \tag{A5}$$

Using the position-dependent form of the chemical potential $\mu_{kx} = \mu_k + RTlnx_k$, a consistent thermodynamic formulation for diffusion current is given as [19]

$$\dot{N}^d{}_k = -\frac{RL}{M_C}\frac{\partial M_C}{\partial x_k} \tag{A6}$$

which by comparison to Equation (A4) yields $L = \frac{DM_C}{R}$. Values of D are widely available [51]. x_k measures position.

In addition to the concentration gradients, the presence of an electric field facilitates ion transport between the two regions. Based on a position- and field potential-dependent chemical potential $\mu_{kx\tau} = \mu_k + RTlnx_k + \tau_k$ to consider the resulting ionic drift (τ_k measures field potential), Einstein related ionic mobility Γ to the diffusion

coefficient D, which in terms of dynamic friction coefficient η (inverse of electrical mobility) and the Boltzmann constant k_B gives the Stokes-Einstein equation for electrical mobility

$$D = \frac{k_B T}{\eta} \tag{A7}$$

Combining diffusion affinity Equation (A3), Fick's law of diffusion Equation (A4), and Stokes-Einstein relation Equation (A6), gives the diffusion-drift work

$$\left(\mu_{high} - \mu_{low}\right) dN^d{}_k = -\frac{k_B R T^2}{\eta} \frac{\partial M_C}{\partial x} dt \ln\left(\frac{m^{low}_{Li+}}{m^{high}_{Li+}}\right) \tag{A8}$$

Adding chemical reaction (Equation (A2)) and ion diffusion-drift (Equation (A7)), gives compositional energy change in the battery

$$\sum \mu_k dN_k = RT\left[\left(K_f - K_r\right) \ln\left(\frac{K_f}{K_r}\right) - \frac{k_B T}{\eta} \frac{\partial M_C}{\partial x} dt \ln\left(\frac{m^{low}_{Li+}}{m^{high}_{Li+}}\right)\right] \tag{A9}$$

which accounts for all primary chemical (reaction) and electrical (transport) kinetics.

A.2. Coupling Reaction and Transport Kinetics with the Electrochemical Potential

Equation (A9) is not convenient for most experimental measurements and performance analyses of a battery in operation. To account for the chemical reactions at the electrodes and the resulting electrical forces in electrolytes, electrochemical potential $\widetilde{\mu}_k = \mu_k + n\prime F\phi$ (a combination of the chemical potential μ_k of the active species k and an electrical field potential ϕ) is typically used to characterize the battery's useful energy, where $n\prime$ is number of species, e.g., electrons, involved in charge transfer (x for lithium-ion batteries, Equations (1) and (2)), $F = 96{,}485$ C/mol is Faraday's constant. Defining electrochemical reaction affinity [19,42] for each electrode half-reaction,

$$\begin{aligned} \widetilde{A}_{ca} &= \mu^{ca}_{Li_{1-x}MO_2} + x\mu^{ca}_{Li^+} + x\mu^{ca}_{e^-} - \mu^{ca}_{LiMO_2} - n\prime F\phi^{ca} \\ \widetilde{A}_{an} &= \mu^{an}_{Li_xC_6} - \mu^{an}_{C_6} - x\mu^{an}_{Li^+} - x\mu^{an}_{e^-} + n'F\phi^{an} \end{aligned} \tag{A10}$$

Summing both half-reactions and rearranging to obtain the overall electrochemical affinity,

$$\widetilde{A} = \mu^{ca}_{Li_{1-x}MO_2} + \mu^{an}_{Li_xC_6} - \mu^{ca}_{LiMO_2} - \mu^{an}_{C_6} + x\left(\mu^{ca}_{Li^+} - \mu^{an}_{Li^+}\right) + x\left(\mu^{ca}_{e^-} - \mu^{an}_{e^-}\right) - n\prime F(\phi^{ca} - \phi^{an}) \tag{A11}$$

For the directly-coupled electrode reactions, the charge potentials cancel out, i.e., $\mu^{ca}_{Li^+} = \mu^{an}_{Li^+}$ and $\mu^{ca}_{e^-} = \mu^{an}_{e^-}$. Rearranging with $\widetilde{A} = 0$ (equilibrium condition) gives the electromotive force or potential difference between both electrodes or the battery's terminal voltage

$$\frac{1}{n\prime F}\left(\mu^{ca}_{Li_{1-x}MO_2} + \mu^{an}_{Li_xC_6} - \mu^{ca}_{LiMO_2} - \mu^{an}_{C_6}\right) = (\phi^{ca} - \phi^{an}) = V \tag{A12}$$

Comparison of the terms in the bracket on the left-hand side of Equation (A12) to the overall reaction in Equation (3), indicates that Equation (A12) could have been derived by directly considering the overall reaction. If $\sum \mu_k = \left(\mu^{ca}_{Li_{1-x}MO_2} + \mu^{an}_{Li_xC_6} - \mu^{ca}_{LiMO_2} - \mu^{an}_{C_6}\right)$ Equation (A12) becomes

$$\frac{1}{n\prime F} \sum \mu_k = V \tag{A13}$$

Equation (A1) and Faraday's law of electrolysis give

$$dN_k = \frac{dq}{n\prime F} \tag{A14}$$

which combines with Equation (A13) to give

$$\sum \mu_k dN_k = V dq \tag{A15}$$

allowing the convenient use of the easily measured terminal voltage V and charge transfer dq or current $I = dq/dt$.

Appendix B

Experimental Results

A battery cycle consisted of discharge followed by charge. The discharge currents were measured as $I = V_R/R_{load}$ (see Figure 2). Constant-charge current of 3 A was used for the charge steps. Using equations for estimating battery capacity and Ohmic work (Joule dissipation in the load resistors), Table A1 presents data from the lithium-ion battery cycling experiments—discharge (left side) and charge (right side). N numbers the discharge–charge cycles. Δt is duration, C_t is accumulated/transferred charge. Other column variables are Ohmic work $W = IV$; battery temperature change $\Delta T = T_{d,c} - T_0$ (subscripts denote end of discharge d, end of charge c, and start of charge/discharge 0); average ambient temperature T_∞ during the discharge/charge; discharge cut-off voltage V_{end}; Thevenin internal impedance $Z = \frac{V_{OC}-V_{CC}}{I}$ determined via open-circuit voltage V_{OC} (measured as V_B with switch open), closed-circuit voltage V_{CC} (measured as V_B with resistive load R_{load} connected to battery), and current I, see Figure 2; and State of Health SoH. Due to varying depths of discharge DoD from cycle to cycle, values at 30 min of discharge are used for Z and SoH in Table A1. Similar trends were observed for all batteries tested [38]. As in Tables 1 and 2, a "Half cycle" is a cycle comprising of a charge step only.

Table A1. Monitored and processed parameters for the Li-ion battery #2 (initial discharge current: ~5 A, charge current: 3 A).

	Discharge								Charge				
N	**Δt h**	**C_t Ah**	**W Wh**	**ΔT degC**	**T_∞ degC**	**V_{end} V**	**$Z_{0.5hr}$ Ω**	**SoH**	**Δt h**	**C_t Ah**	**W Wh**	**ΔT degC**	**T_∞ degC**
1	1.47	−6.10	−19.9	6.5	25.9	0.77	0.042	1.00	3.49	10.47	41.4	0.2	27.6
2	1.79	−8.37	−28.6	10.2	24.8	2.43	0.025	0.98	1.72	5.14	20.2	0.8	26.7
3	Half cycle								1.33	3.97	16.1	8.1	25.7
4	2.00	−9.52	−32.9	6.2	27.8	2.66	0.031	0.98	1.28	3.83	15.1	−2.7	27.7
5	0.64	−3.00	−10.2	8.6	24.6	2.69	0.081	0.95	1.81	5.42	21.8	−0.3	26.5
6	1.53	−7.23	−24.6	7.2	26.1	2.61	0.026	0.97	1.47	4.41	17.4	0.4	26.7
7	1.40	−6.71	−22.9	6.8	24.8	2.67	0.032	0.99	2.73	8.17	32.8	0.0	25.3
8	2.03	−9.74	−33.4	8.8	24.6	2.64	0.028	1.00	Missing data				
9	1.36	−6.39	−21.5	6.3	24.9	2.58	0.026	0.98	3.60	10.80	43.3	2.6	27.1
10	1.77	−8.70	−30.3	7.1	26.8	2.87	0.024	0.99	0.61	1.81	7.0	−1.7	27.7
11	1.09	−5.18	−17.5	9.2	23.5	2.42	0.027	0.99	1.62	4.86	19.2	0.9	26.2
12	1.82	−8.52	−29.0	6.9	26.6	1.88	0.032	0.99	1.80	5.40	21.5	2.8	26.3
13	Half cycle								2.13	6.37	25.3	−0.7	28.5
14	2.12	−10.54	−37.0	6.3	29.7	2.32	0.028	1.03	0.99	2.96	11.5	−0.7	29.5
15	1.33	−6.24	−21.0	8.8	24.7	2.42	0.040	0.98	1.53	4.58	18.1	−0.1	26.7
16	1.73	−8.27	−28.1	7.9	24.8	2.14	0.025	1.00	1.46	4.38	17.3	−0.7	25.8
17	1.67	−7.97	−27.0	8.9	25.4	2.31	0.029	1.00	1.81	5.42	21.5	−0.5	27.5
18	2.13	−10.01	−33.6	7.3	26.2	1.46	0.027	1.02	1.28	3.84	15.0	0.7	27.5
19	1.36	−6.42	−21.4	5.6	25.6	2.18	0.026	0.99	1.47	4.40	17.4	−0.6	26.1
20	2.00	−8.95	−29.2	8.0	25.8	0.95	0.027	1.01	1.69	5.06	20.1	0.1	28.2
21	2.16	−9.45	−30.4	9.0	27.2	1.10	0.028	1.02	1.27	3.79	14.9	−0.1	26.7
22	1.50	−6.78	−21.8	7.4	25.6	1.58	0.031	0.98	1.41	4.22	16.7	0.9	25.8
23	1.74	−7.85	−25.8	5.9	25.3	1.93	0.021	0.95	1.50	4.50	17.8	2.0	26.0
24	1.80	−8.19	−26.7	11.1	24.0	1.68	0.025	0.97	1.73	5.17	20.5	−0.2	26.5
25	0.68	−3.35	−11.7	3.4	25.6	3.44	0.025	0.97	4.16	12.47	50.9	2.1	26.3
26	2.69	−12.37	−40.6	8.0	25.0	1.56	0.036	1.00	1.48	4.43	17.5	2.4	26.8
27	2.44	−8.84	−25.7	6.9	24.9	0.57	0.034	0.95	2.76	8.27	33.1	3.1	26.7
28	Half cycle								1.77	5.30	21.1	3.1	26.3
29	1.91	−6.41	−18.1	8.4	25.5	0.58	0.045	0.93	3.08	9.22	37.2	2.3	25.9
30	0.91	−3.75	−11.4	13.0	25.2	1.15	0.074	0.96	3.33	9.97	40.4	2.7	26.3
31	1.31	−5.76	−17.7	8.3	25.8	1.80	0.051	0.95	3.21	9.63	39.2	7.2	26.1
32	0.75	−3.19	−9.7	12.3	25.4	1.51	0.129	0.94	1.69	5.05	20.0	0.9	25.7

References

1. Rahn, C.D.; Wang, C.Y. *Battery Systems Engineering*, 1st ed.; John Wiley & Sons Ltd.: Hoboken, NJ, USA, 2013. [CrossRef]

2. Huggins, R.A. *Energy Storage: Fundamentals, Materials and Applications*, 2nd ed.; Springer: New York, NY, USA, 2010. [CrossRef]
3. Ménard, L.; Fontès, G.; Astier, S. Dynamic energy model of a lithium-ion battery. *Math. Comput. Simul.* **2010**, *81*, 327–339. [CrossRef]
4. Bresser, D.; Paillard, E.; Passerini, S. Lithium-ion batteries (LIBs) for medium- and large-scale energy storage: Current cell materials and components. In *Advances in Batteries for Medium and Large-Scale Energy Storage*; Elsevier Ltd.: Amsterdam, The Netherlands, 2014; Volume 1, pp. 125–211. [CrossRef]
5. Goodenough, J.B. Energy storage materials: A perspective. *Energy Storage Mater.* **2015**, *1*, 158–161. [CrossRef]
6. Bresser, D.; Paillard, E.; Passerini, S. Lithium-ion batteries (LIBs) for medium- and large-scale energy storage: Emerging cell materials and components. In *Advances in Batteries for Medium and Large-Scale Energy Storage*; Menictas, C., Skyllas-Kazacos, M., Lim, T.M., Eds.; Elsevier Ltd.: Amsterdam, The Netherlands, 2014; Volume 1, pp. 213–289. [CrossRef]
7. Kurzweil, P. Lithium battery energy storage: State of the art including lithium-air and lithium-sulfur systems. In *Electrochemical Energy Storage for Renewable Sources and Grid Balancing*, 1st ed.; Moseley, P.T., Garche, G., Eds.; Elsevier B.V.: Amsterdam, The Netherlands, 2014; pp. 269–307. [CrossRef]
8. Goodenough, J.B.; Kim, Y. Challenges for rechargeable batteries. *J. Power Sources* **2011**, *196*, 6688–6694. [CrossRef]
9. Scrosati, B.; Garche, J. Lithium batteries: Status, prospects and future. *J. Power Sources* **2010**, *195*, 2419–2430. [CrossRef]
10. Vetter, J.; Novák, P.; Wagner, M.R.; Veit, C.; Möller, K.C.; Besenhard, J.O.; Winter, M.; Wohlfahrt-Mehrens, M.; Vogler, C.; Hammouche, A. Ageing mechanisms in lithium-ion batteries. *J. Power Sources* **2005**, *147*, 269–281. [CrossRef]
11. Jiang, J.; Zhang, C. *Fundamentals and Applications of Lithium-Ion Batteries in Electric Drive Vehicles*; John Wiley & Sons Singapore Pte Ltd.: Singapore, 2015. [CrossRef]
12. Barsukov, Y. Challenges and Solutions in Battery Fuel Gauging; 2004. Available online: http://www.ti.com/lit/ml/slyp086/slyp086.pdf (accessed on 29 March 2019).
13. Miranda, D.; Costa, C.M.; Lanceros-Mendez, S. Lithium ion rechargeable batteries: State of the art and future needs of microscopic theoretical models and simulations. *J. Electroanal. Chem.* **2015**, *739*, 97–110. [CrossRef]
14. Ecker, M.; Gerschler, J.B.; Vogel, J.; Käbitz, S.; Hust, F.; Dechent, P.; Sauer, D.U. Development of a lifetime prediction model for lithium-ion batteries based on extended accelerated aging test data. *J. Power Sources* **2012**, *215*, 248–257. [CrossRef]
15. Cordoba-Arenas, A.; Onori, S.; Guezennec, Y.; Rizzoni, G. Capacity and power fade cycle-life model for plug-in hybrid electric vehicle lithium-ion battery cells containing blended spinel and layered-oxide positive electrodes. *J. Power Sources* **2015**, *278*, 473–483. [CrossRef]
16. Panchal, S.; McGrory, J.; Kong, J.; Dincer, I.; Agelin-Chaab, M.; Fraser, R.; Fowler, M. Cycling degradation testing and analysis of a $LiFePO_4$ battery at actual conditions. *Int. J. Energy Res.* **2017**, *41*, 2565–2575. [CrossRef]
17. Panchal, S.; Rashid, M.; Long, F.; Mathew, M.; Fraser, R.; Fowler, M. *Degradation Testing and Modeling of 200 Ah $LiFePO_4$ Battery*; SAE Technical Paper; SAE International: Detroit, MI, USA, 2018. [CrossRef]
18. Karnopp, D. Bond graph models for electrochemical energy storage: Electrical, chemical and thermal effects. *J. Frankl. Inst.* **1990**, *327*, 983–992. [CrossRef]
19. Kondepudi, D.; Prigogine, I. *Modern Thermodynamics: From Heat Engines to Dissipative Structures*; John Wiley & Sons Ltd.: Hoboken, NJ, USA, 1998.
20. Esperilla, J.J.; Félez, J.; Romero, G.; Carretero, A. A full model for simulation of electrochemical cells including complex behavior. *J. Power Sources* **2007**, *165*, 436–445. [CrossRef]
21. Ramadass, P.; Haran, B.; White, R.; Popov, B.N. Capacity fade of Sony 18650 cells cycled at elevated temperatures: Part II. Capacity fade analysis. *J. Power Sources* **2002**, *112*, 614–620. [CrossRef]
22. Feng, X.; Gooi, H.B.; Chen, S. Capacity fade-based energy management for lithium-ion batteries used in PV systems. *Electr. Power Syst. Res.* **2015**, *129*, 150–159. [CrossRef]
23. Ashwin, T.R.; Chung, Y.M.; Wang, J. Capacity fade modelling of lithium-ion battery under cyclic loading conditions. *J. Power Sources* **2016**, *328*, 586–598. [CrossRef]
24. Long, L.; Wang, S.; Xiao, M.; Meng, Y. Polymer electrolytes for lithium polymer batteries. *J. Mater. Chem. A* **2016**, *4*, 10038–10069. [CrossRef]

25. Schmalstieg, J.; Käbitz, S.; Ecker, M.; Sauer, D.U. A holistic aging model for Li(NiMnCo)O_2 based 18650 lithium-ion batteries. *J. Power Sources* **2014**, *257*, 325–334. [CrossRef]
26. Ecker, M.; Nieto, N.; Käbitz, S.; Schmalstieg, J.; Blanke, H.; Warnecke, A.; Sauer, D.U. Calendar and cycle life study of Li(NiMnCo)O_2-based 18650 lithium-ion batteries. *J. Power Sources* **2014**, *248*, 839–851. [CrossRef]
27. Käbitz, S.; Gerschler, J.B.; Ecker, M.; Yurdagel, Y.; Emmermacher, B.; André, D.; Mitsch, T.; Sauer, D.U. Cycle and calendar life study of a graphite|LiNi1/3Mn 1/3Co1/3O2 Li-ion high energy system. Part A: Full cell characterization. *J. Power Sources* **2013**, *239*, 572–583. [CrossRef]
28. Bryant, M.D.; Khonsari, M.M.; Ling, F.F. On the thermodynamics of degradation. *Proc. R. Soc. A: Math. Phys. Eng. Sci.* **2008**, *464*, 2001–2014. [CrossRef]
29. Strutt, J.W.; Rayleigh, B. The Theory of Sound. *Nature* **1877**, *2*. [CrossRef]
30. Onsager, L. Reciprocal Relations in Irreversible processes. *Phys. Rev.* **1931**, *37*, 405. [CrossRef]
31. Doelling, K.L.; Ling, F.F.; Bryant, M.D.; Heilman, B.P. An experimental study of the correlation between wear and entropy flow in machinery components. *J. Appl. Phys.* **2000**, *88*, 2999–3003. [CrossRef]
32. Ling, F.F.; Bryant, M.D.; Doelling, K.L. On irreversible thermodynamics for wear prediction. *Wear* **2002**, *253*, 1165–1172. [CrossRef]
33. Bryant, M.D. Entropy and Dissipative Processes of Friction and Wear. *FME Trans.* **2009**, *37*, 55–60.
34. Bryant, M.D. On Constitutive Relations for Friction from Thermodynamics and Dynamics. *J. Tribol.* **2016**, *138*, 041603. [CrossRef]
35. Naderi, M.; Khonsari, M.M. An experimental approach to low-cycle fatigue damage based on thermodynamic entropy. *Int. J. Solids Struct.* **2010**, *47*, 875–880. [CrossRef]
36. Amiri, M.; Modarres, M. An entropy-based damage characterization. *Entropy* **2014**, *16*, 6434–6463. [CrossRef]
37. Amiri, M.; Naderi, M.; Khonsari, M.M. An experimental approach to evaluate the critical damage. *Int. J. Damage Mech.* **2011**, *20*, 89–112. [CrossRef]
38. Osara, J.A. The Thermodynamics of Degradation. Ph.D. Thesis, The University of Texas at Austin, Austin, TX, USA, May 2017.
39. DeHoff, R.T. *Thermodynamics in Material Science*, 2nd ed.; CRC Press: Boca Raton, FL, USA, 2006.
40. Callen, H.B. *Thermodynamics and an Introduction to Thermostatistics*; John Wiley & Sons, Ltd.: Hoboken, NJ, USA, 1985.
41. De Groot, S.R. *Thermodynamics of Irreversible Processes*; North-Holland Publishing Company: Amsterdam, The Netherland, 1951. [CrossRef]
42. Prigogine, I. *Introduction to Thermodynamics of Irreversible Processes*; Charles C Thomas: Springfield, IL, USA, 1955.
43. Bejan, A. *Advanced Engineering Thermodynamics*, 3rd ed.; John Wiley & Sons, Inc.: Hoboken, NJ, USA, 1997.
44. Moran, M.J.; Shapiro, H.N. *Fundamentals of Engineering Thermodynamics*, 5th ed.; Wiley: Hoboken, NJ, USA, 2004.
45. Burghardt, M.D.; Harbach, J.A. *Engineering Thermodynamics*, 4th ed.; Harper Collins College Publishers: Glenview, IL, USA, 1993.
46. Reynier, Y.; Yazami, R.; Fultz, B. The entropy and enthalpy of lithium intercalation into graphite. *J. Power Sources* **2003**, *119–121*, 850–855. [CrossRef]
47. Yazami, R.; Maher, K. Thermodynamics of lithium-ion batteries. In *Lithium-Ion Batteries: Advances and Applications*; Pistoia, G., Ed.; Elsevier: Amsterdam, The Netherlands, 2014. [CrossRef]
48. Bejan, A. The method of entropy generation minimization. In *Energy and the Environment*; Sage Publications: Thousand Oaks, CA, USA, 1990; pp. 11–22.
49. Pal, R. Demystification of the Gouy-Stodola theorem of thermodynamics for closed systems. *Int. J. Mech. Eng. Educ.* **2017**, *45*, 142–153. [CrossRef]
50. Fernández, I.J.; Calvillo, C.F.; Sánchez-Miralles, A.; Boal, J. Capacity fade and aging models for electric batteries and optimal charging strategy for electric vehicles. *Energy* **2013**, *60*, 35–43. [CrossRef]
51. Lide, D.R. *CRC Handbook of Chemistry and Physics*, 75th ed.; CRC Press: Boca Raton, FL, USA, 1994.